Influences of the Monsoon Trough and Arabian Heat Low on Summer Rainfall over the United Arab Emirates

DANIEL F. STEINHOFF, ROELOF BRUINTJES, JOSHUA HACKER,[a] TEDDIE KELLER, CHRISTOPHER WILLIAMS, AND TARA JENSEN

Research Applications Laboratory, National Center for Atmospheric Research, Boulder, Colorado

ABDULLA AL MANDOUS AND OMAR A. AL YAZEEDI

National Center of Meteorology, Abu Dhabi, United Arab Emirates

(Manuscript received 11 October 2017, in final form 12 February 2018)

ABSTRACT

The factors responsible for rare summertime rainfall over portions of the United Arab Emirates (UAE), which have not been previously explored in detail, are elucidated with the Climate Forecast System Reanalysis and WRF mesoscale model simulations. The simulations show associations between active phases of the southwest Asian monsoon and intensification of the Arabian heat low, leading up to UAE rainfall events. Variability in the location and strength of the Arabian heat low circulation, which differs from the static portrayal in climatological minimum sea level pressure (MSLP), can affect the development of deep convection over the UAE. Analysis of the vorticity equation for a two-day case study period confirms that convergence is solely responsible for the spinup and maintenance of the primary heat low circulation. Convergence is also responsible for the spinup of a separate cyclonic circulation over the eastern UAE, which propagates offshore to the Arabian Gulf during morning hours. This cyclonic circulation advects moist air onshore over the western UAE, and deep convection follows from inland horizontal convective rolls and interaction with the approaching sea-breeze front. The development of widespread deep convection is shown to be most favorable during the decay phase of the Arabian heat low, when the preconditioned moist air is not replaced by drier continental flow, and the vertical profiles of temperature and moisture are also more favorable. Three other rainfall cases are briefly discussed to illustrate how the strength and geographic position of the Arabian heat low can affect rainfall characteristics over the UAE.

1. Introduction

During summertime, the climate of the United Arab Emirates (UAE) and much of the Arabian Peninsula is dominated by the Arabian heat low (AHL), sea/land breezes, and large-scale subsidence associated with the subtropical belt of high pressure in the upper troposphere that extends from northern Africa across southern Asia (e.g., Krishnamurti et al. 2013). Summer is the driest period of the year for the UAE, with rainfall in many locations and years being nonexistent or contributing little to the annual rainfall average, estimated between 78 mm (FAO 1997; Ouarda et al. 2014) and 110 mm (Sherif et al. 2014). Spatially, the annual average ranges from 40 mm over the southern desert region to 160 mm over the northeastern mountains (FAO 1997; Ouarda et al. 2014), although this range varies among different global precipitation products (Wehbe et al. 2017). Interannual variability of rainfall is high, with the standard deviation being 75%–85% of the annual rainfall average (Sherif et al. 2014). The intra-annual temporal variability is even larger during summer and over the western desert regions of the UAE, as the impact of frontal systems and orographic effects are eliminated, respectively. Global-scale teleconnections are associated with interannual variability in UAE rainfall (Kumar and Ouarda 2014; Ouarda et al. 2014; Chandran et al. 2016), but the physical mechanisms responsible for highly episodic summertime rainfall over a region with otherwise persistent weather conditions remain unexplained. These episodic summertime rainfall

[a] Current affiliation: Jupiter Technology Systems, Boulder, Colorado.

Corresponding author: Daniel F. Steinhoff, steinhof@ucar.edu

DOI: 10.1175/MWR-D-17-0296.1

events can have a substantial influence on the regional hydrology.

Heat lows (also referred to as thermal lows or thermal troughs) are prevalent over warm season desert regions across the world [see Warner (2004) for a sampling of heat low studies delineated by region]. Specific to the Arabian Peninsula, the vertical structure of the AHL has been studied observationally by Ackerman and Cox (1982), Blake et al. (1983), and Smith (1986a,b). The minimum pressure of the heat low is observed during afternoon hours, with maximum pressure during late morning. The cyclonic circulation, upward vertical motion, and mass convergence associated with the heat low are generally confined to the layer beneath 850 hPa, with an anticyclonic outflow layer between 850 hPa and 700 hPa and weak convergence aloft. Downward vertical motion is prevalent above the daytime 850-hPa level. The daytime mixed layer extends from the surface to 650–550 hPa.

While there is a net radiative loss to outer space above the heat low, the heat low itself is a total energy source region for the atmosphere. An important factor in the radiative budget of the heat low is the effect of dust aerosols toward the warming of the midtroposphere (Ackerman and Cox 1982; Mohalfi et al. 1998). The overall energy surplus of the heat low is exported to the western Arabian Sea by the lower-tropospheric divergent outflow and is hypothesized to be a key feature of the southwest Asian monsoon system (Krishnamurti et al. 2013).

Numerical studies complement the observational studies of heat lows. Rácz and Smith (1999) and Spengler and Smith (2008) ran idealized simulations to study the dynamics of heat lows. They found that the heat low is not in quasigeostrophic balance, as the minimum surface pressure occurs during late afternoon or early evening, whereas the relative cyclonic vorticity maximizes during early-morning hours. The overlying anticyclone is in approximate gradient wind balance, is strongest in the lower troposphere, and has little diurnal variation.

Low-level convergence associated with the deepening heat low results from the sea breeze during daytime and a low-level jet at night (Rácz and Smith 1999). Thermally forced circulations—in particular, sea breezes and land breezes—are also climatological features of the UAE and much of the Arabian Peninsula. Reviews of sea-breeze studies are widely available (e.g., Simpson 1994; Miller et al. 2003; Crosman and Horel 2010). Sea-breeze circulations form because of surface temperature and heat capacity contrasts between adjacent land and water surfaces during daytime conditions. The near-surface air temperature gradient across land and sea results in a thermally direct circulation (from Bjerknes' circulation theorem) and onshore flow. The thermal gradient reverses at night, resulting in an offshore land-breeze circulation. Climatological studies of sea/land breezes over the Arabian Gulf region using observations (Eager et al. 2008) and numerical simulation (Zhu and Atkinson 2004) find that sea breezes occur year-round but are most pronounced during summer, when they occur on 96%–99% of days. The typical daily inland extent of the sea breeze is about 160 km, and the onshore flow extends to 750–1500 m AGL.

Over land, daytime boundary layer convection is often organized into quasi-two-dimensional features called horizontal convective rolls (HCRs). Reviews of HCRs and boundary layer convective structures in general can be found in Etling and Brown (1993), Atkinson and Zhang (1996), and Young et al. (2002). HCR formation is dependent upon adequate surface sensible heat flux and near-surface vertical wind shear (Weckwerth et al. 1997). The structure of HCRs—whether they are linear rolls, convective cells, or are unorganized—is primarily determined by z_i/L, where z_i is the boundary layer depth, and L is the Obukhov length (Weckwerth et al. 1999). The positioning of roll updrafts and downdrafts can impact the formation of deep convection (Weckwerth et al. 1996; Weckwerth 2000). Additionally, convective precipitation can form due to interactions between the sea-breeze front (SBF; the leading edge of the marine flow) and HCRs that form in the boundary layer inland (Wakimoto and Atkins 1994; Atkins et al. 1995; Dailey and Fovell 1999; Fovell and Dailey 2001; Fovell 2005). Convection is initiated above an HCR updraft ahead of the SBF. The SBF and HCRs have complementary required roles in the development of deep convection: the SBF provides uplift and moisture to the inland environment, and the HCRs transport moisture upward through both the roll updraft and gravity waves that form in the return flow just above the HCR.

Colloquially, nonorographic summertime rainfall over the western UAE is attributed to convergence between the sea breeze and southerly flow on the eastern flank of the AHL. However, the infrequent and isolated nature of rainfall events, in stark contrast to the persistence of the sea breeze and the AHL in summer, suggests that specific conditions due to the variability of these features are important for the generation of rainfall. In this study, it is shown that intensification of the southwest Asian monsoon trough over the northern Arabian Sea results in a more vigorous AHL circulation that modifies lower-tropospheric moisture transport over the UAE, providing favorable conditions for the development of deep convection. The focus here is on the western UAE, as the eastern UAE features complex topography that influences summertime rainfall events,

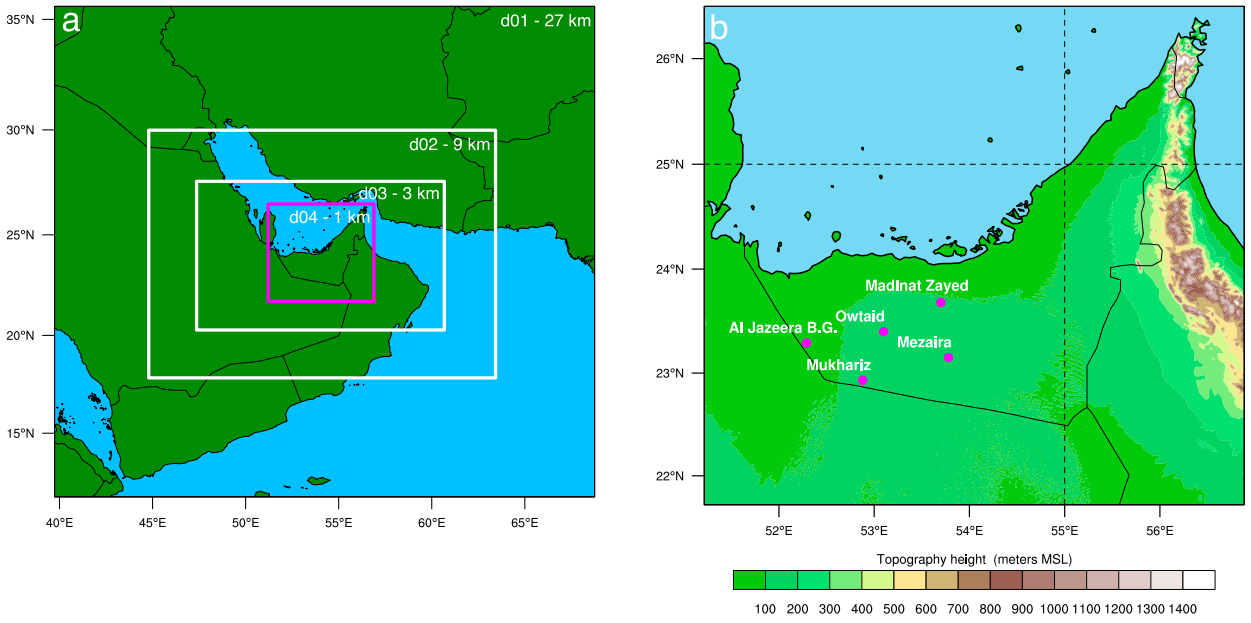

FIG. 1. (a) Map of the WRF domain nesting structure used for simulations in this study. (b) The 1-km domain inset [indicated by magenta in (a)] with terrain height (shaded contours; m) and the five western UAE stations used in the analysis, indicated by magenta-filled circles.

warranting further analysis beyond the scope of this study.

2. Data and methods

a. Reanalysis

Reanalysis data are used for the study of the synoptic-scale setup of rain days (section 3) and the case study vorticity analysis of the AHL (section 4a). The National Centers for Environmental Prediction (NCEP) Climate Forecast System Reanalysis (CFSR; Saha et al. 2010a) is a coupled Earth system model that includes the atmosphere, ocean, land surface, and sea ice. CFSR uses the three-dimensional variational data assimilation (3D-Var) Gridpoint Statistical Interpolation (GSI) analysis system (Kleist et al. 2009) for initial conditions and ingests a wide array of conventional observations and satellite radiance observations. The CFSR atmospheric component features spectral T382 (~0.31°) horizontal resolution with 64 vertical levels. CFSR was extended beyond 2010 with the NCEP Climate Forecast System version 2 (CFSv2; Saha et al. 2014). CFSR and CFSv2 output is obtained from the NCAR Research Data Archive (Saha et al. 2010b,c, 2011a,b). Output on a 720 × 361 0.5° latitude–longitude grid is primarily used here, with 0.205° × ~0.204° Gaussian grid output used for case study plots of 2-m specific humidity and 10-m winds. To estimate the statistical significance of differences in reanalysis fields between climatology and a subset of western UAE rain days, a 10 000-member bootstrap (with replacement) is used, comprising subsamples of 40 distinct 3-day time periods (the 3 days are consecutive), mimicking the 1–3-day lag associated with the 40 rain days analyzed in section 3.

b. Weather Research and Forecasting Model

Output from the Advanced Research version of Weather Research and Forecasting (WRF-ARW; Skamarock et al. 2008) Model is used in study of the sea-breeze front and convection for the case studies in section 4b. WRF solves for the nonhydrostatic Euler equations on a spatially discretized grid in the horizontal and a terrain-following hydrostatic pressure vertical coordinate. WRF-ARW version 3.7.1 is used in this study. A nesting structure of 27, 9, 3, and 1 km is used for the spatial domains, which is shown in Fig. 1a. The 1-km domain is used for analysis, which is shown with terrain height in Fig. 1b. There are 74 vertical levels up to 50 hPa. An adaptive time-stepping scheme is used for all domains, starting at $5 \times \Delta x$ and ranging between 1 and $6 \times \Delta x$, targeting a domain-wide CFL criterion of 1.2. CFSR output from the NCAR Research Data Archive (see previous section) is used for input and lateral boundary conditions, along with updating SST, vegetation fraction, and surface albedo, at 6-hourly intervals using 6-h forecast fields.

Extensive options exist for parameterizing physical processes outside of the model dynamical core, and the

options used in this study are presented here. The Lin cloud microphysics scheme (Lin et al. 1983; Chen and Sun 2001) is used, which is a single-moment scheme with six classes of hydrometeors. This scheme performed better in simulating realistic accumulated rainfall for the isolated convective precipitation events analyzed in this study, as other schemes severely underestimated rainfall amounts. Rajeevan et al. (2010) compare four microphysics schemes (including the Lin scheme) in a simulation of a severe thunderstorm event over southeast India in WRF and find that the Lin scheme correctly simulates more rainfall than the other schemes tested. The Rapid Radiative Transfer Model for GCMs (RRTMG; Iacono et al. 2008) is used for both shortwave and longwave spectral bands. The Mellor–Yamada–Janjić (MYJ) planetary boundary layer (PBL) scheme (Janjić 1994) is used for the estimation of subgrid-scale turbulent fluxes. MYJ is a TKE-based scheme, which has been shown to better simulate deep convection than countergradient schemes for a case where a lower-tropospheric reservoir of moisture is important for cloud development, due to differences in the vertical mixing of moisture throughout the boundary layer (Burton et al. 2013). This lower-tropospheric reservoir of moisture will be shown to be a key feature for deep convection in this study. Corresponding to the MYJ PBL scheme is the Eta surface layer scheme. The Noah land surface model (Chen and Dudhia 2001) is used, which has four soil layers and a fractional (mosaic) land-cover distribution for each grid point. The MODIS 15-s 20-category land-use dataset is used, along with the USGS 30-s terrain height (27-, 9-, and 3-km domains) and the SRTM 90-m terrain height (1-km domain) datasets. The Tiedtke convective parameterization scheme (Tiedtke 1989; Zhang et al. 2011) is used for the 27- and 9-km domains.

c. Observations

Surface observations, upper-air soundings, and radar data are used for the case study overview and model validation, and they were obtained from the UAE National Center of Meteorology and Seismology (NCMS) and cover the 2003–14 time period. Data were quality controlled by NCMS staff and the authors prior to use. Near-surface temperature, relative humidity, station pressure, wind (speed and direction), incident solar radiation, and precipitation are available from a network of automatic weather station (AWS) and airport weather station locations. To focus on the climatology of the inland western UAE for analysis purposes of this study, a subset of five stations (Al Jazeera B.G., Madinat Zayed, Mezaira, Mukhariz, and Owtaid) is used, the locations of which are indicated in Fig. 1b.

Measurable rainfall was observed at one or more stations on 40 days during July–August for the time period analyzed. Radar data for Abu Dhabi, Al Ain, Dubai, and Mezaira are used for days when return echoes were present.

d. Vorticity analysis

To describe the evolution of the AHL, a form of the vorticity tendency equation that allows for the characterization of the circulation associated with the heat low is employed. The vorticity equation in flux form is used (Haynes and McIntyre 1987; Raymond and López-Carrillo 2011; Tory et al. 2012; Raymond et al. 2014; Smith et al. 2015; Kilroy et al. 2016). In isobaric coordinates, it can be stated as

$$\frac{\partial \zeta_a}{\partial t} = -\nabla_h \cdot \mathbf{Z}, \tag{1}$$

where ζ_a is the vertical component of absolute vorticity (hereafter,"absolute vorticity"), and the subscript h represents an operator or variable on an isobaric surface. The term $\mathbf{Z}$ is the horizontal flux of the absolute vorticity, defined as

$$\mathbf{Z} = \mathbf{v}_h \zeta_a - \boldsymbol{\zeta}_h \omega + \mathbf{k} \times \mathbf{F}, \tag{2}$$

where $\mathbf{v}_h$ is velocity, ω represents vertical motion in isobaric coordinates, and $\mathbf{F}$ is the Reynolds stress vector. Equation (1) states that the time tendency of absolute vorticity is equal to the convergence of the horizontal flux of absolute vorticity.

Applying the divergence operator to (2) results in three forcing terms. The first term is convergence of the advective flux and can be expanded as

$$-\nabla_h \cdot (\mathbf{v}_h \zeta_a) = -\mathbf{v}_h \cdot \nabla_h \zeta_a - \zeta_a \delta, \tag{3}$$

where δ is divergence. The first term on the rhs of (3) is the advection of absolute vorticity by the horizontal wind, and the second term represents the stretching effect from mass convergence. The remaining terms on the rhs of (2) are nonadvective flux terms, and when the divergence operator is applied, the second term on the rhs of (2) represents tilting. The third term represents turbulent dissipation in the boundary layer (bulk friction). Detailed physical interpretation of the three forcing terms can be found in Raymond et al. (2014). The advantages of interpreting the vorticity equation as in (1) are explained by Raymond and López-Carrillo (2011), Raymond et al. (2014), and Smith et al. (2015). An increase in the concentration of vorticity in (1) results in an increase in the circulation of the vortex through the stretching term, as mass continuity requires

convergence. The advection term of (3) redistributes areas of vorticity but does not create or destroy it. Area integration of (1), applying Green's theorem to the left-hand side and applying the divergence theorem to the right-hand side, results in

$$\frac{d\Gamma}{dt} = -\oint_{dA} \mathbf{Z}\, d\mathbf{l}, \tag{4}$$

where Γ is the absolute circulation and is defined as the line integral around a defined area A, with $d\mathbf{l}$ being the displacement vector along the edge of A. Changes to the concentration of vorticity along the periphery of A, through the forcing terms in (2), determine the time tendency of total circulation. The circulation tendency is estimated through area integration of (1).

CFSR output is used for the vorticity analysis. The 950-hPa pressure level is used, which is always above the ground over nonmountainous areas of the Arabian Peninsula. Vorticity, divergence, and horizontal gradients are computed using spherical harmonics, while vertical gradients are computed using centered differences (25-hPa spacing). Similar to Raymond and López-Carrillo (2011), and based on a daytime well-mixed boundary layer, $\mathbf{F}$ in (2) is estimated using a bulk aerodynamic formula:

$$\mathbf{F} \approx \frac{\boldsymbol{\tau}}{z_s}, \tag{5}$$

where $\boldsymbol{\tau}$ is the turbulent momentum flux, and z_s is the PBL height, with both variables obtained directly from CFSR output (the former at 10-m height). Because of the modest lateral movement of the heat low circulations, the calculations are performed in a fixed frame of reference.

3. Synoptic-scale setup of rain days

In this section, the synoptic-scale composite charts for conditions prior to the 40 rain days over the western UAE are analyzed to ascertain features that are relevant for rainfall there. Figures 2a–c show CFSR 500-hPa geopotential height and wind vector plots for the July–August 2003–14 climatology, the rain-day composites at 1–3-day lag, and the differences between the rain-day composites and the climatology. The 2003–14 period coincides with available observations used in this study. The 1–3-day lag represents all 6-hourly CFSR time steps that are 1–3 days before the days with measurable rainfall at western UAE sites. The choice of days 1–3 before the rain day was based on a sensitivity study of each day in isolation (not shown) and is used to represent the prerequisite circulations that lead to favorable conditions for deep convection, shown in the next section.

Both the climatology (Fig. 2a) and lagged rain-day composite (Fig. 2b) show the extension of the Saharan high across Saudi Arabia and Iran, a representation of the monsoon trough over western India and the northern Arabian Sea, and northeasterly flow over the eastern Arabian Peninsula. However, the lagged rain-day composite chart shows a contraction of the climatological high over Iran and, to a lesser extent, over the Arabian Peninsula, illustrated in the difference plot (Fig. 2c). Negative height anomalies are also present over the monsoon trough.

Figures 2d–f show similar climatology, composite, and anomaly plots for minimum sea level pressure (MSLP) and 10-m wind vectors. The climatology (Fig. 2d) illustrates the AHL, the Arabian Gulf pressure trough (Bitan and Sa'Aroni 1992), the Somali jet over the Arabian Sea, and areas of low pressure over portions of Afghanistan, Pakistan, and northwestern India. Climatological northwesterly flow over the Arabian Gulf and representation of the cyclonic circulation of the AHL are apparent. The lagged rain-day composite (Fig. 2e) and difference (Fig. 2f) show an intensified AHL, with negative pressure anomalies centered over Saudi Arabia but extending across the entire Arabian Peninsula. The monsoon trough over the northern Arabian Sea is strengthened, and the low over Pakistan and northwestern India (the ''Pak–India'' low; Bollasina and Nigam 2011) is weaker.

The climatology of 2-m specific humidity (Fig. 2g) shows a gradient of moisture across the Arabian Peninsula, with southerly flow bringing increased low-level moisture along the eastern flank of the AHL. The lagged rain-day composite (Fig. 2h) and anomalies (Fig. 2i) show enhanced low-level moisture and southerly flow over much of the Arabian Peninsula. Northwesterly flow is weaker, and specific humidity is higher, over the Arabian Gulf in the lagged rain-day composite.

The discussion above illustrates an intensification of both the monsoon trough over the northern Arabian Sea and the AHL leading up to rain days. A connection between the trough and the heat low has been previously hypothesized. Smith (1986a) analyzed near-surface meteorological observations taken over the Saudi Arabian Empty Quarter during summer 1981 and attributed increases of near-surface relative humidity and temperature that occur on time scales of a few days to an intensification of the AHL. He suggested that either 1) the intensity of daytime surface heating increases, or 2) subsidence warming increases over the heat low [resulting from enhanced convection to the south or east, as described by Ramage (1966)]. The latter hypothesis

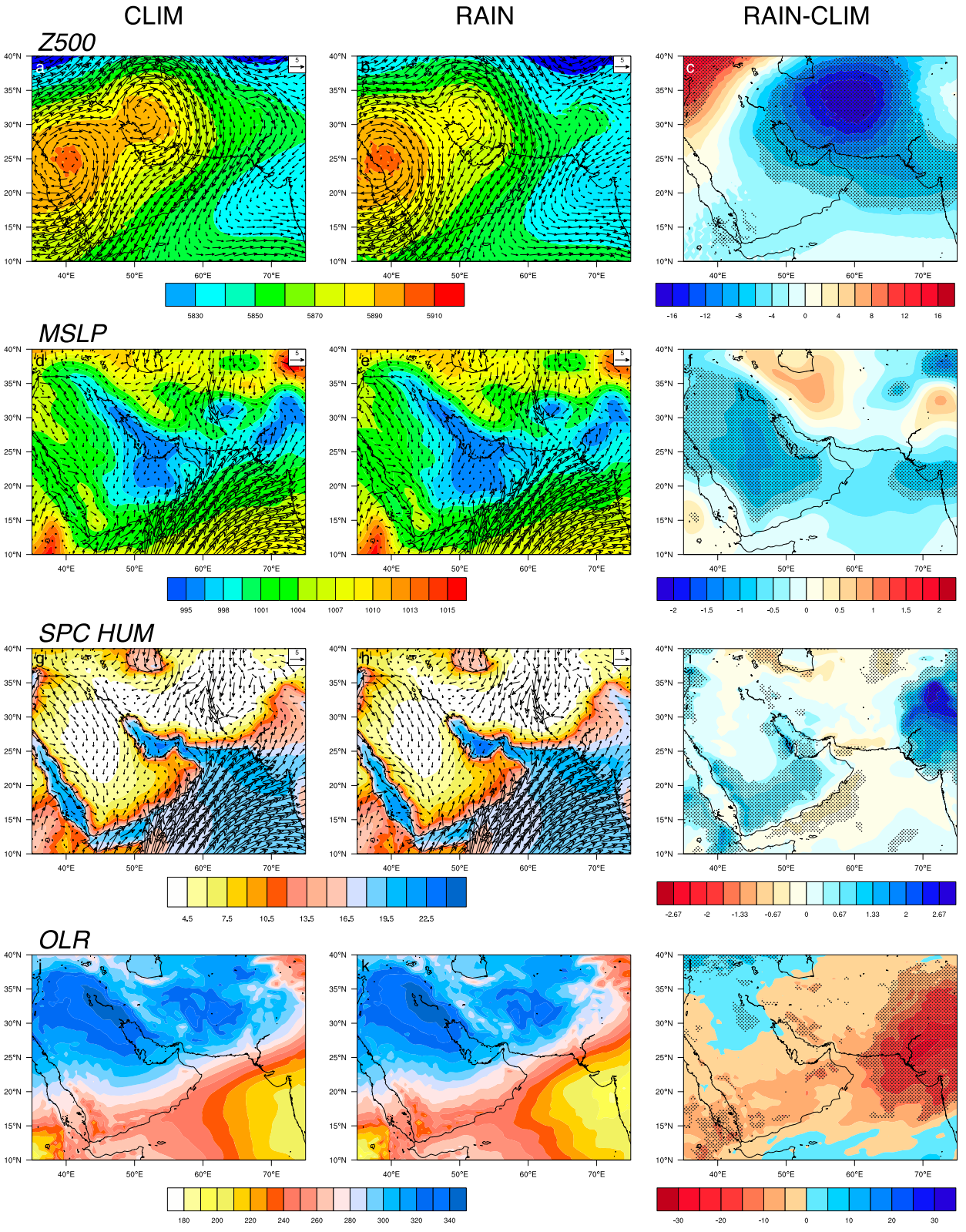

FIG. 2. (a) CFSR climatology, (b) rain-day composites, and (c) rain-day anomalies for 500-hPa geopotential height (hPa) and winds (reference vector is 5 m s^{-1}). (d)–(f) As in (a)–(c), but for MSLP (hPa) and 10-m winds. (g)–(i) As in (a)–(c), but for 2-m specific humidity (g kg^{-1}) and 10-m winds. (j)–(l) As in (a)–(c), but for OLR (W m^{-2}). Stippled areas in difference plots represent bootstrapped statistical significance at the 97.5% level.

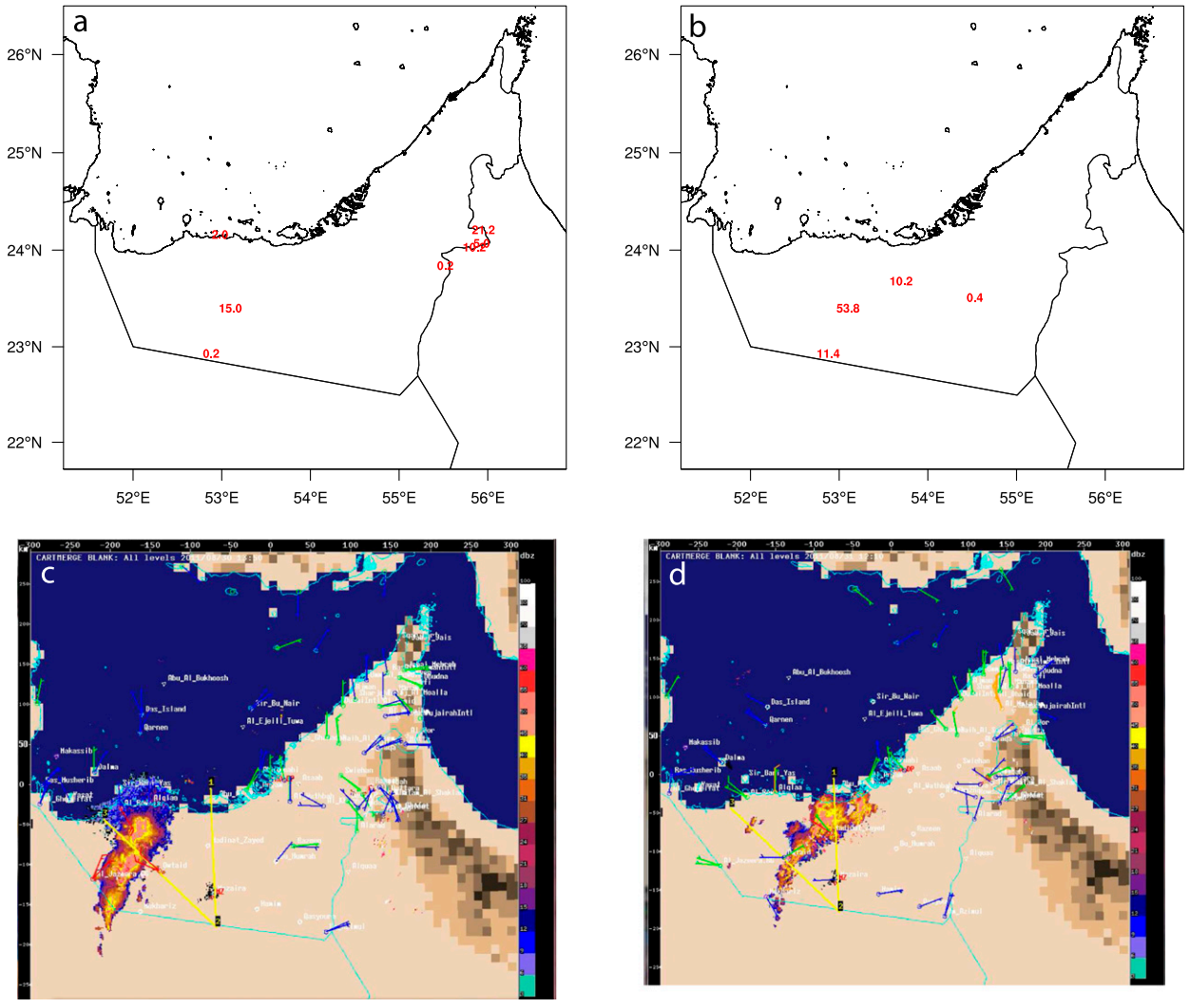

FIG. 3. Observed rainfall amounts (mm) for (a) 30 and (b) 31 Aug 2011 and radar reflectivity for (c) 1350 UTC 30 Aug and (d) 1210 UTC 31 Aug 2011.

would imply that enhanced convection associated with the monsoon trough over the northern Arabian Sea leads to a stronger AHL through a more vigorous indirect circulation.

Figure 2j shows the climatological top of the atmosphere outgoing longwave radiation (OLR). Lower OLR values over portions of India and over the Arabian Sea represent convection associated with the monsoon. Lagged rain-day composite OLR in Fig. 2k shows lower OLR over the northern Arabian Sea and northwestern India. The lagged rain-day composite OLR anomalies (Fig. 2l) are similar in structure to active monsoon rainfall composite OLR anomalies in Gadgil and Joseph (2003). This northwestern expansion of the monsoon trough increases diabatic heating aloft, and climatological upper-tropospheric easterlies then advect the warm air to the Arabian Peninsula. Subsidence over the heat low (Blake et al. 1983) results in strengthened outflow above the heat low, greater convergence at the surface, and spinup of the heat low through the vorticity equation. The enhanced heat low circulation associated with rain days results in lower MSLP (Fig. 2f) and also enhanced near-surface humidity (Fig. 2i) due to stronger onshore flow on the eastern flank of the heat low.

4. Case study of 30–31 August 2011

This section presents a detailed analysis of two consecutive days characterized by intense rainfall. First, vorticity spinup associated with the heat low and an additional cyclonic circulation feature over the Arabian Gulf is assessed. The effects of these cyclonic features

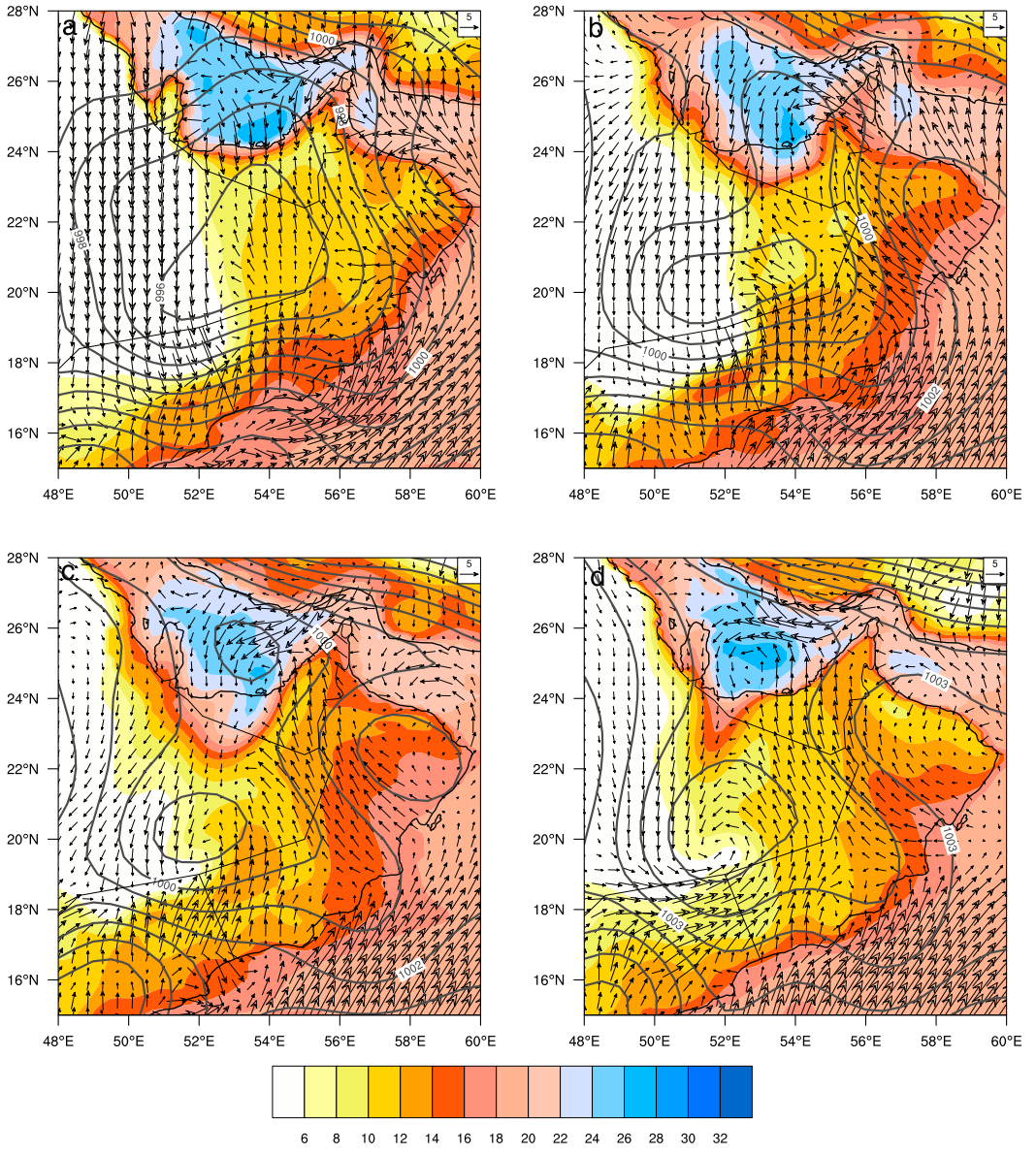

FIG. 4. MSLP (contours; hPa), 2-m specific humidity (color shading; g kg^{-1}), and 10-m wind vectors from CFSR at (a) 1200 and (b) 1800 UTC 29 Aug 2011 and (c) 0000 and (d) 0600 UTC 30 Aug 2011.

toward the development of deep convection are then explored.

Rainfall amounts from AWS sites over the UAE for 30 and 31 August 2011 are shown in Figs. 3a and 3b, respectively. The aggregate rainfall amounts across all observing sites for these days are the sixth and fourth largest recorded for July–August 2003–14. When only western UAE stations are considered, these days are the fourth and first largest rainfall amounts over the observed record. Using consecutive days is advantageous for comparing and contrasting the rain days, as the synoptic-scale meteorological patterns are very similar. Figures 3c and 3d show sample radar returns from both days, illustrating the general location of convection. Rainfall is concentrated over western UAE stations on 30 August (excluding rainfall over the far eastern UAE), whereas rainfall is more widely distributed on 31 August.

a. Vorticity analysis

Figure 4 shows the evolution of the AHL with MSLP, 10-m wind vectors, and 2-m specific humidity at 1200 UTC 29 August, 1800 UTC 29 August, 0000 UTC 30 August, and 0600 UTC 30 August. At 1200 UTC (Fig. 4a), there is a clear signature of the heat low circulation over

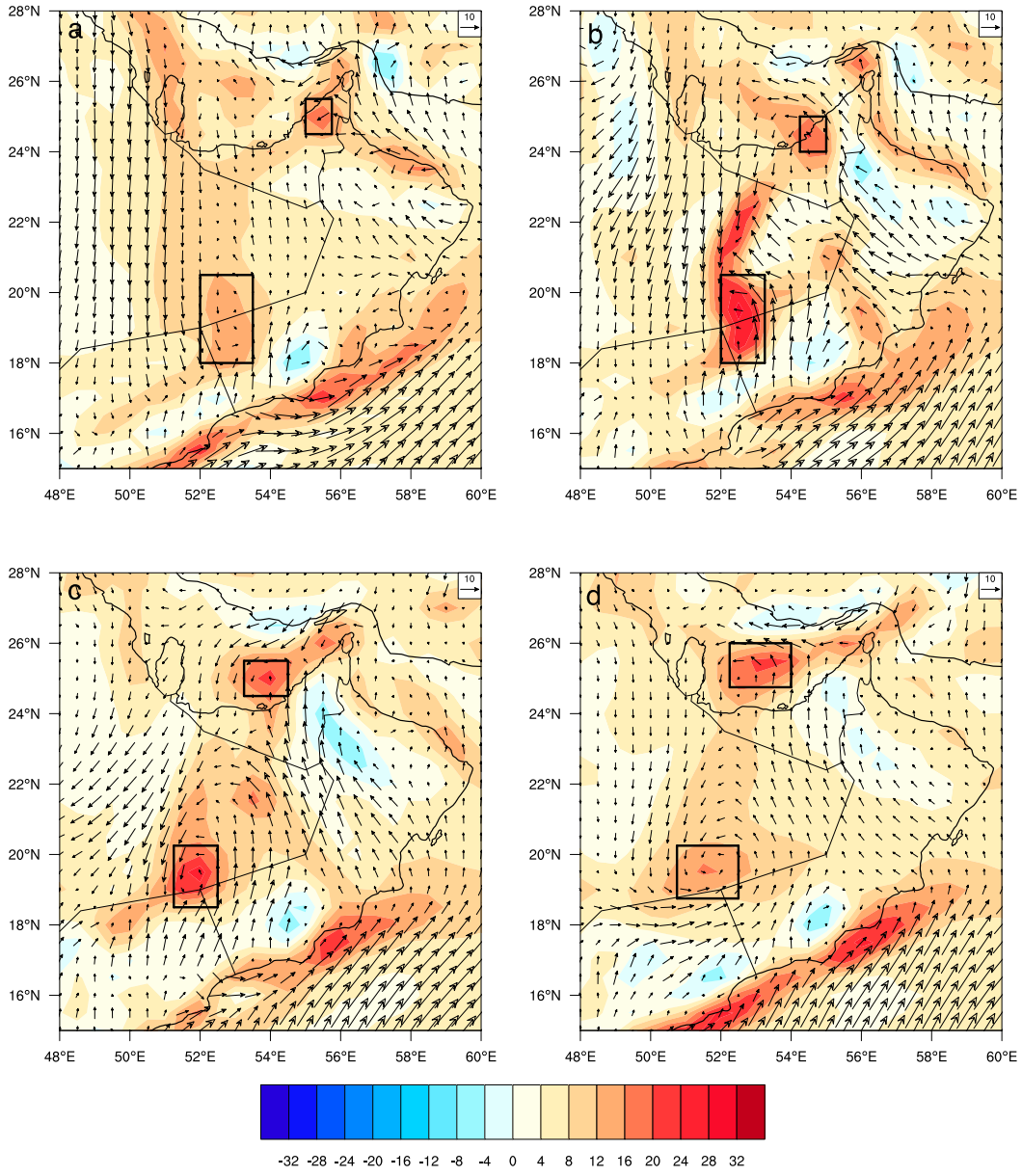

FIG. 5. Vertical component of absolute vorticity (10^{-5} s^{-1}; color shading) and wind vectors at 950 hPa at (a) 1200 and (b) 1800 UTC 29 Aug 2011 and (c) 0000 and (d) 0600 UTC 30 Aug 2011. Black boxes represent areas used for vorticity analysis in Fig. 6.

the Empty Quarter, which is not always apparent during daytime because of strong boundary layer convection and sea-breeze circulations, even in idealized simulations (Rácz and Smith 1999). The heat low MSLP is below 996 hPa and displaced northward from the cyclonic circulation. Throughout the time period analyzed, lower-tropospheric moisture is advected northward on the eastern flank of the AHL.

By 1800 UTC (Fig. 4b), onshore flow has intensified across the eastern Arabian Peninsula, and the cyclonic circulation around the heat low becomes more coherent over the Empty Quarter, while the MSLP increases. Moist onshore flow extends farther inland, along the eastern flank of the AHL. By 0000 UTC (Fig. 4c), the heat low circulation is better defined over the Empty Quarter as MSLP continues to increase, and a cyclonic circulation is also evident over the southern Arabian Gulf, with moist onshore flow continuing along the eastern flank of the AHL. The pattern is similar 6 h later at 0600 UTC (Fig. 4d), as the heat low circulation

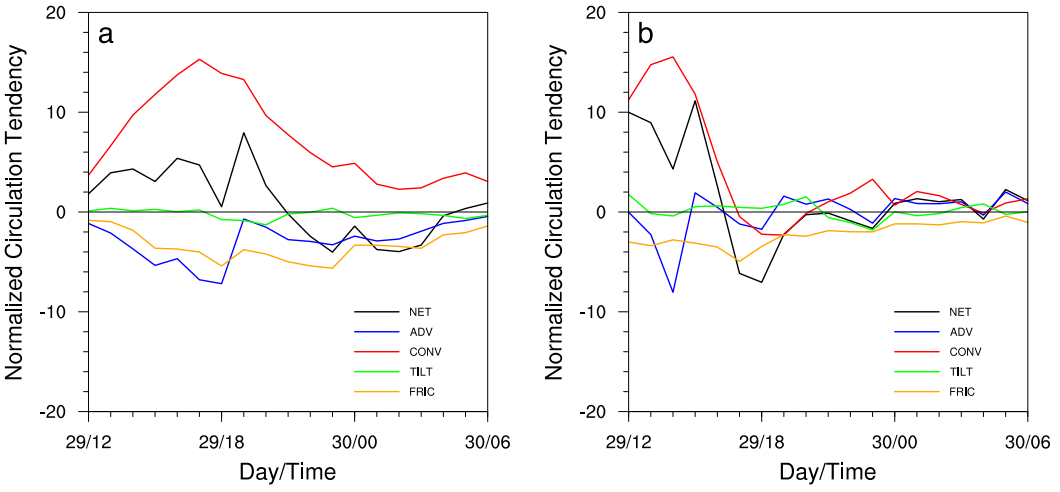

FIG. 6. Vorticity analysis of the normalized circulation tendency ($km\,s^{-1}\,day^{-1}$; normalized to the area of a $1° \times 1°$ box) for (a) the primary heat low and (b) Arabian Gulf circulation boxes in Fig. 5. See text for description of terms.

encompasses much of the Arabian Peninsula, and the cyclonic circulation over the Arabian Gulf has propagated westward.

The MSLP climatology and lagged rain-day composite in Figs. 2d and 2e indicate a single minimum over the eastern Arabian Peninsula that is identified as the AHL. As previously explained (Rácz and Smith 1999; Spengler and Smith 2008), the heat low is not in quasigeostrophic balance. Figure 4 also shows that separate cyclonic circulations can form over the northern and southern sections of the Arabian Peninsula.

While mass convergence appears to be favorable for the development of cyclonic vorticity, an analysis of the vorticity equation ascertains the forcing of the vorticity tendency, as described in section 2d. Figures 5a–d show 950-hPa absolute vorticity and wind vectors at 1200 UTC 29 August, 1800 UTC 29 August, 0000 UTC 30 August, and 0600 UTC 30 August. The black boxes in Fig. 5 denote the approximate area of the cyclonic circulations associated with the heat low and the area over which the vorticity analysis is performed. Figure 6 shows the hourly vorticity analysis for the (Fig. 6a) primary heat low circulation and (Fig. 6b) Arabian Gulf circulation, where "NET" is the net forcing from (1), "ADV" and "CONV" are the horizontal advection and convergence terms from the first rhs term in (2) and expanded in (3), "TILT" is the tilting term [second rhs term in (2)], and "FRIC" is the friction term [third rhs term in (2)].

The primary heat low circulation (Fig. 6a) intensifies through 2100 UTC, almost exclusively from the convergence term. Negative vorticity advection and frictional spin-down primarily oppose the convergence term. After 2100 UTC, the circulation weakens as the convergence term becomes smaller. The Arabian Gulf circulation (Fig. 6b) intensifies from mass convergence through daytime hours, weakens briefly, and then stabilizes after 1800 UTC. During this time, the advection due to the offshore flow over the eastern UAE has a small positive effect on the circulation tendency.

The vorticity analysis in Fig. 6 illustrates the importance of mass convergence in the generation of the cyclonic circulations, which is not surprising when a scale analysis of the vorticity equation is considered (e.g., Holton 1992; Martin 2006). Convergence and cyclonic vorticity generation is concentrated where the preexisting heat low circulation and sea-breeze flows intersect (Figs. 4, 5). The convergence term remains positive throughout the analysis period for the southern circulation, as the heat low approaches quasigeostrophic balance. Convergence is primarily a daytime effect for the northern circulation, driven by onshore flow from the Arabian Gulf and the Gulf of Oman. Weak mass convergence and advection sustain this circulation through overnight hours over the Arabian Gulf. An intensified heat low effect—as described in section 3 (Fig. 2i)—is primarily responsible for the enhanced onshore flow and generation of cyclonic circulations that persist through overnight hours.

The cyclonic circulation over the Arabian Gulf that forms overnight creates favorable conditions for convection the next day over the western UAE in two ways. First, moist air is advected onshore overnight and during early-morning hours. This preconditions the lower troposphere with moist air, in contrast to a thermally forced land breeze during quiescent conditions. Second, the closed cyclonic circulation prevents intrusion of dry continental air over the Arabian Gulf, allowing for the

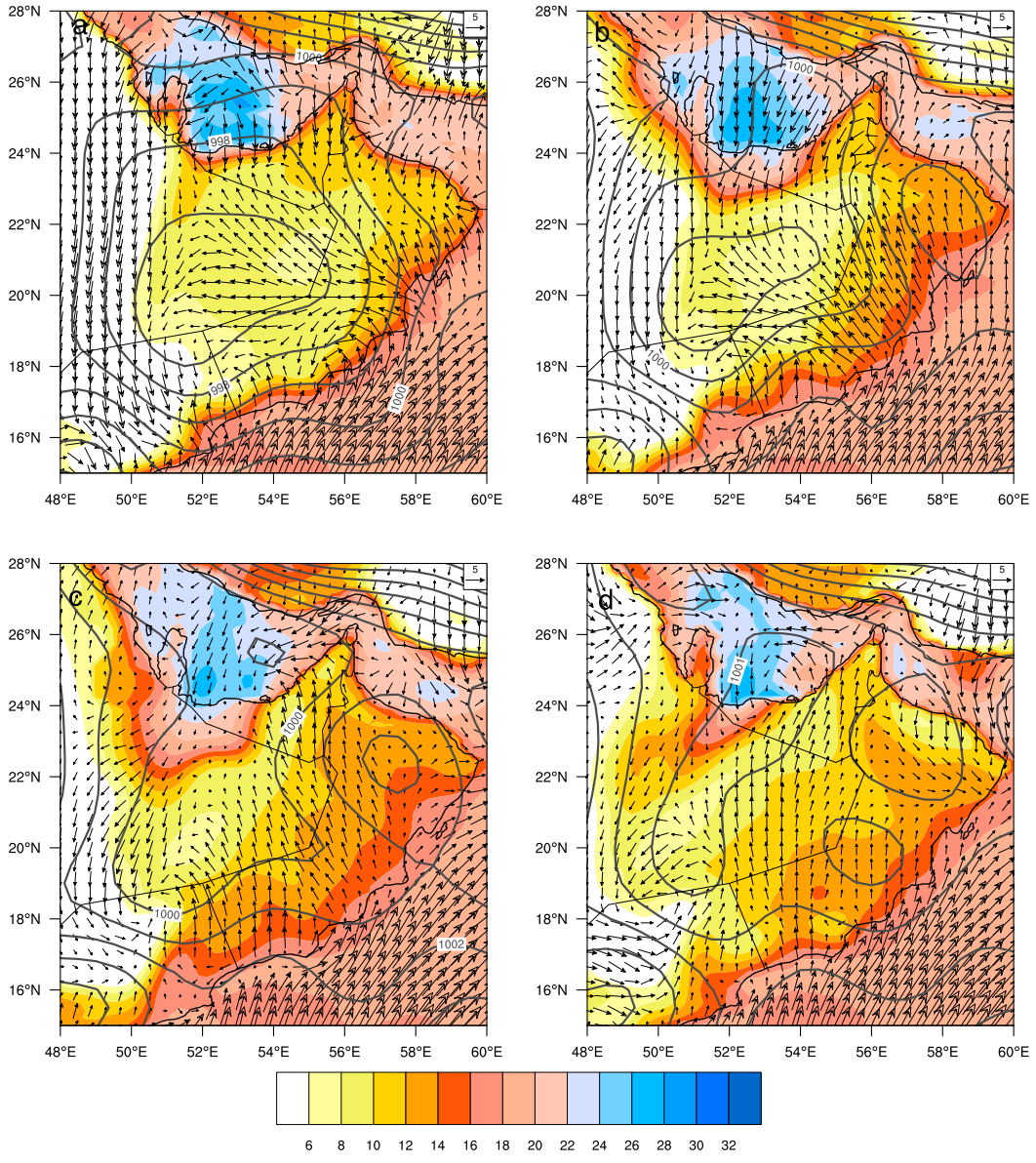

FIG. 7. MSLP (contours; hPa), 2-m specific humidity (color shading; g kg^{-1}), and 10-m wind vectors from CFSR at (a) 1200 and (b) 1800 UTC 30 Aug 2011 and (c) 0000 and (d) 0600 UTC 31 Aug 2011.

advection of moist low-level air onshore over the western UAE.

A similar analysis is presented for 31 August 2011 to illustrate similarities to the day before that lead to rainfall and differences that lead to more intense convection. Figures 7a–d show MSLP, 10-m wind vectors, and 2-m specific humidity at 1200 UTC 30 August, 1800 UTC 30 August, 0000 UTC 31 August, and 0600 UTC 31 August. Separate cyclonic circulations, one associated with the heat low and one over the Arabian Gulf, are again apparent overnight. Similar to Fig. 4, the heat low is deepest at 1200 UTC and fills in thereafter. Also, onshore flow again exists throughout the time period over the western UAE. The strength of the onshore flow across the Arabian Peninsula, the depth of the heat low, and the MSLP gradient are all weaker than the previous day.

Figures 8a–d show 950-hPa absolute vorticity and wind vectors at 1200 UTC 30 August, 1800 UTC 30 August, 0000 UTC 31 August, and 0600 UTC 31 August, and Fig. 9 shows the hourly vorticity analysis for (Fig. 9a) the primary heat low and (Fig. 9b) the Arabian Gulf circulations. Both circulations are weaker than the day before, but are again strengthened during daytime hours by mass

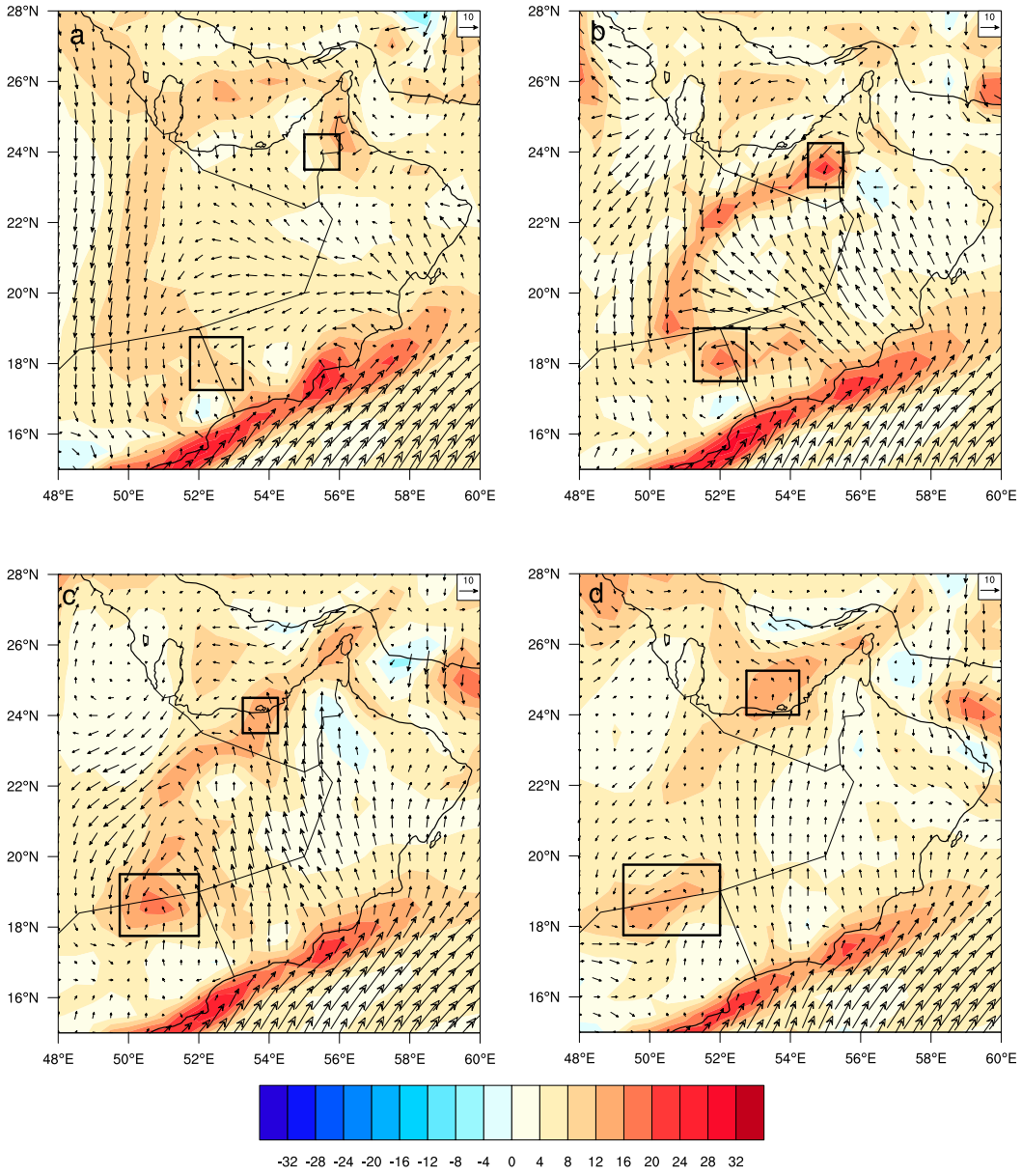

FIG. 8. Vertical component of absolute vorticity (10^{-5} s^{-1}; color shading) and wind vectors at 950 hPa at (a) 1200 and (b) 1800 UTC 30 Aug 2011 and (c) 0000 and (d) 0600 UTC 31 Aug 2011. Black boxes represent areas used for vorticity analysis in Fig. 9.

convergence before weakening overnight. Advection and friction are dominant negative forcing terms for the primary heat low circulation, while advection has a positive effect for the Arabian Gulf circulation between 2100 and 0000 UTC, as the circulation moves westward over the Gulf. While similarities in the evolution of both cyclonic circulations leading into the rain days are apparent, the heat low and sea-breeze features are weaker for the 31 August 2011 case. Several other factors compensate for the weaker heat low, discussed next, leading to more intense and widespread convection on 31 August 2011.

b. Convection

The conditions leading to convective precipitation over the western UAE on 30–31 August 2011 are now explored. Figure 10a shows 2-m specific humidity and 10-m wind vectors from WRF at 0900 UTC 30 August (1300 local time). The cyclonic circulation over the Arabian Gulf advects moist air inland, over the far

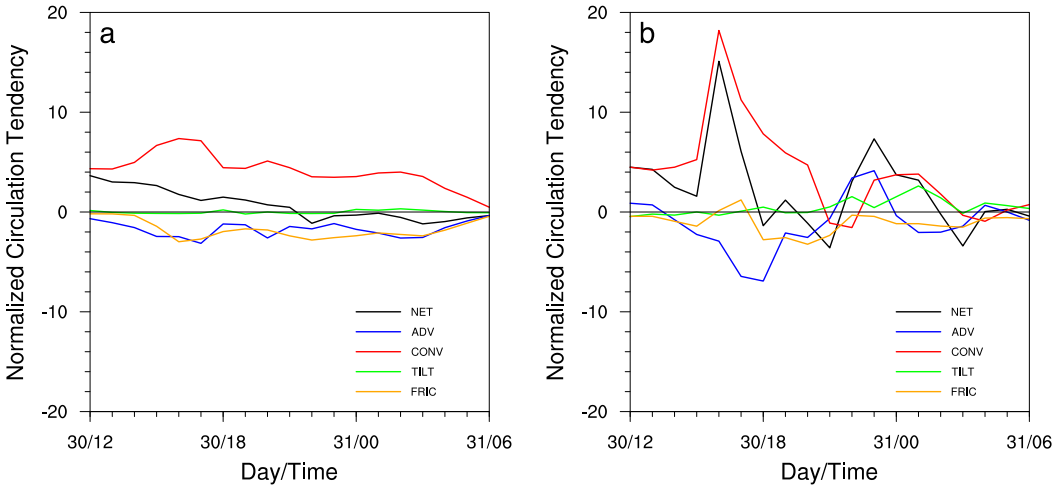

FIG. 9. Vorticity analysis of the normalized circulation tendency ($km\,s^{-1}\,day^{-1}$; normalized to the area of a $1° \times 1°$ box) for (a) the primary heat low and (b) Arabian Gulf circulation boxes in Fig. 8. See text for description of terms.

western UAE. Southeasterly flow exists over areas to the east, associated with the primary heat low circulation. A zonally oriented moisture gradient of nearly $15\,g\,kg^{-1}$ extends across 100 km of the western UAE at similar distances from the coast. Figure 10b shows the specific humidity field from the AWS stations (interpolated to a spatial field using a triangular mesh) and wind barbs at 0900 UTC 30 August. Comparing Figs. 10a and 10b, the moist tongue of air over the western UAE, representation of the northern edge of the primary heat low circulation over the southern UAE, and representation of the cyclonic circulation over the Arabian Gulf are common features between WRF and the AWS observations. Figure 11a shows a vertical cross section through the onshore flow over the western UAE. The moist marine layer extends to about 1 km above mean sea level (MSL), with the onshore flow being shallower (under 500 m). Offshore flow exists aloft, which is broader (spatially and vertically) than what a sea-breeze return flow would be. Boundary layer convection is beginning to form inland of the sea-breeze front, which is located at approximately $X = 90$ km.

The heat low is weaker and displaced farther from the UAE on 31 August, compared to the day before (cf. Figs. 4, 7). Once again, the Arabian Gulf circulation advects moist air over the western UAE throughout the night and early-morning hours. Figure 10c shows 2-m specific humidity and 10-m wind vectors from WRF at 0900 UTC 31 August (1300 local time). Compared to 24 h earlier, the cyclonic circulation over the Arabian Gulf is displaced southeast, so that the moist onshore flow extends farther east. Also, with the primary heat low circulation being weaker and displaced southwest, flow over the rest of the UAE is weaker and westerly. This results in a broader area of higher specific humidity over the western UAE, as the preconditioned moist air is not displaced by the drier continental flow.

Drier conditions exist over areas not impacted by the onshore flow. Figure 10d shows AWS observations of specific humidity and wind barbs at 0900 UTC 31 August. The enhanced moisture over the western UAE, the westerly flow over the southern UAE, cyclonic circulation over the Arabian Gulf, and the drier conditions over the interior of the UAE, compared to the day before, are consistent between WRF and observations.

When comparing the vertical cross section at 0900 UTC 31 August (Fig. 11b) with that of 24 h earlier (Fig. 11a), the vertical depth of the offshore moist air layer is shallower, but the horizontal convective rolls are stronger. The SBF is more diffuse, and the stability just ahead of the SBF is weaker. Figure 12a shows a comparison of soundings from WRF just ahead of the SBF at 0900 UTC 30 and 31 August, and Table 1 shows corresponding sounding parameters from WRF. While the near-surface mixing ratio is similar between the cases, and both cases feature well-mixed boundary layers up to about 2 km MSL, the sounding at 0900 UTC 31 August is slightly warmer in the PBL. Combined with a larger increase in stability just above the PBL, moderate CIN and a higher LFC are apparent at 0900 UTC 30 August. Deep convection develops near the sounding location for 0900 UTC 31 August within the hour, whereas convection begins 2 h later on 30 August.

One hour later at 1000 UTC 30 August, the SBF continues to sharpen as it propagates inland, and drier air is advected from the southeast (Fig. 13a). The preconditioned moist air from the morning continues to be displaced by drier air. The moist air over the

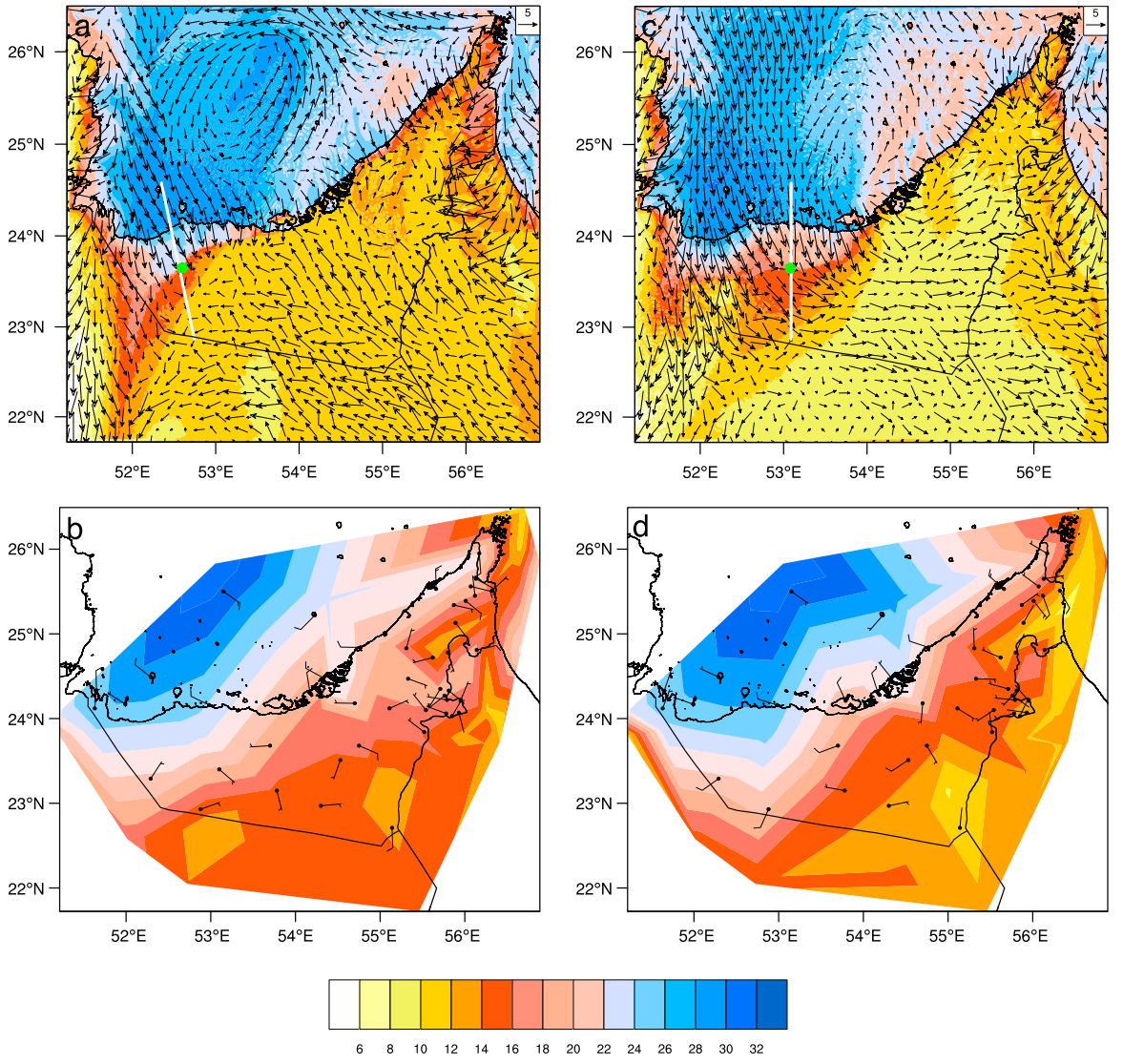

FIG. 10. (a) WRF 2-m specific humidity (color shading; g kg^{-1}) and 10-m wind vectors at 0900 UTC 30 Aug 2011; (b) AWS observations of specific humidity interpolated to a triangular mesh (color shading) and wind vectors at 0900 UTC 30 Aug 2011; (c),(d) as in (a) and (b), respectively, but for 0900 UTC 31 Aug 2011.

western UAE is again represented in AWS observations (Fig. 13b), although the inland extent of the northwesterly flow over the western UAE may be underestimated in the WRF simulations.

At 1000 UTC 31 August (Fig. 13c), the preconditioned moist air is simply advected eastward as the SBF remains diffuse. Deep convection has already formed just behind the SBF. Figure 12b shows a comparison of soundings from WRF at an identical geographic location ahead of the SBF, with Table 1 showing corresponding sounding parameters from WRF. This represents conditions that the SBF and/or outflow boundaries will encounter, so the feasibility for the development of convection is assessed. The temperature profiles through the PBL of about 3 km are nearly identical, but the mixing ratio in the PBL is several grams per kilogram higher at 1000 UTC 31 August. While neither case has any CIN, the LFC is about 1 km higher, and CAPE is over 1000 J kg^{-1} lower, at 1000 UTC 30 August.

5. Other cases

Other rain days show similar patterns of an intensified AHL and overnight onshore flow, but differences in position and strength of the AHL lead to variability in the characteristics of deep convection, compared to the

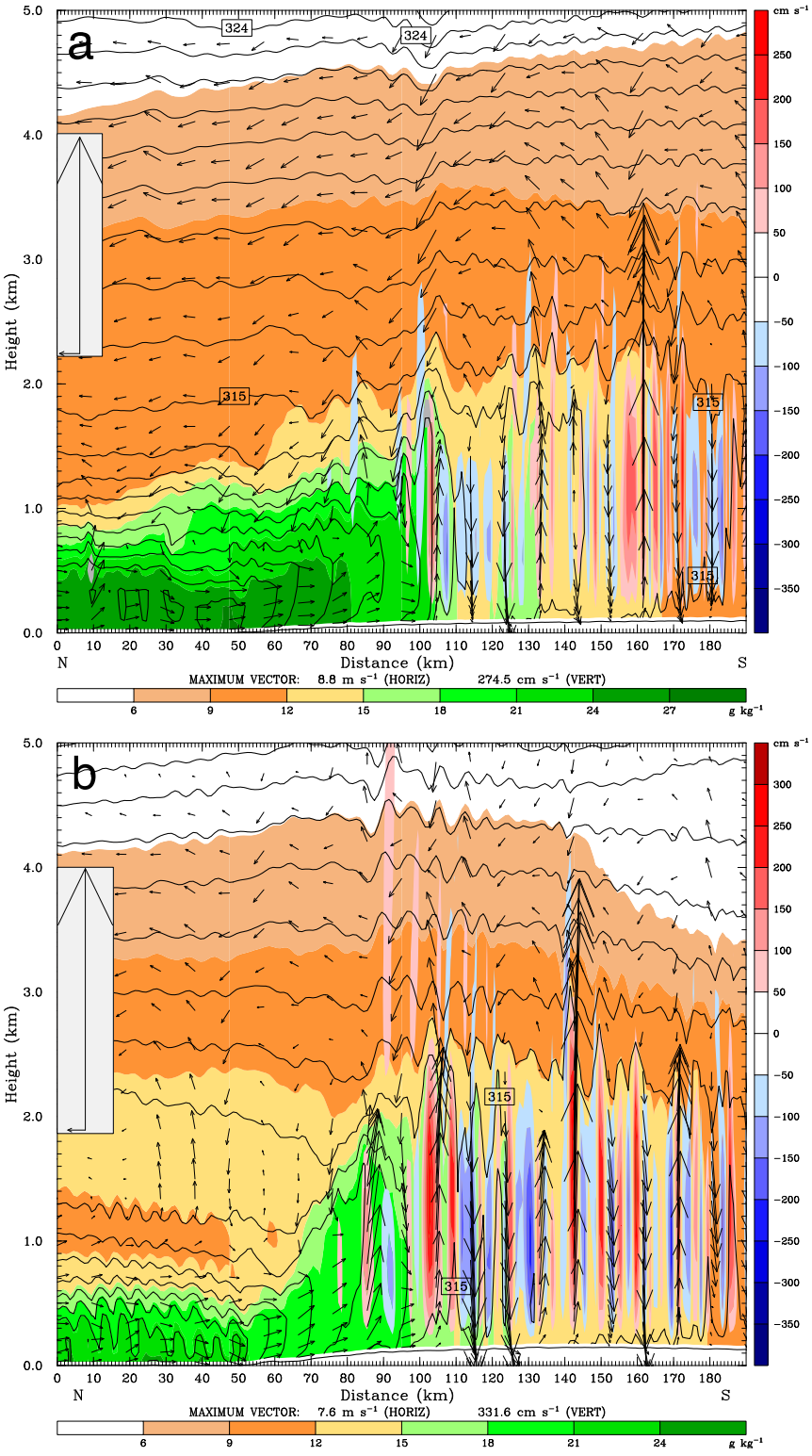

FIG. 11. (a) WRF vertical cross-section of potential temperature (contours; K), specific humidity (color shading using scale at bottom of plot; g kg^{-1}), vertical velocity (color shading using scale to right of plot; cm s^{-1}), and circulation vectors (with reference vector on left edge of plot) corresponding to the white line in Fig. 10a at 0900 UTC 30 Aug 2011. (b) As in (a), but for the white line in Fig. 10c at 0900 UTC 31 Aug 2011.

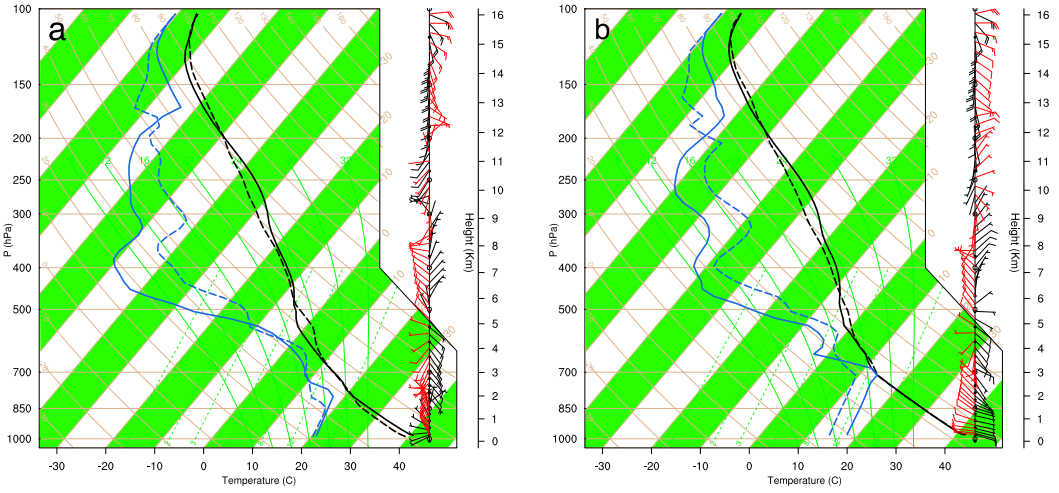

FIG. 12. (a) Thermodynamic diagram showing vertical profiles of temperature (black), dewpoint temperature (blue), and winds at locations represented by green dots in Fig. 10a at 0900 UTC 30 Aug 2011 (dashed lines and black wind barbs) and Fig. 10b at 0900 UTC 31 Aug 2011 (solid lines and red wind barbs). (b) As in (a), but for 1000 UTC and at locations represented by green dots in Figs. 13a and 13c. The CAPE, CIN, and LFC values for these soundings are listed in Table 1.

cases detailed earlier. Here, three other rainfall days are used to illustrate these effects. Figure 14 shows MSLP, 10-m wind vectors, and 2-m specific humidity at 0600 UTC 10 August (Fig. 14a) and 12 August 2013 (Fig. 14b). When the western UAE station subset is considered, 10 August 2013 is the second largest rain day, while no rainfall was measured at these sites on 12 August 2013.

Figure 14a shows an Arabian heat low displaced northward, compared to the days analyzed in the previous section, and several hectopascals lower. The cyclonic circulation over the Arabian Gulf is in a similar position to 31 August, bringing moist onshore flow across the western UAE. Correspondingly, rainfall was extensive across the UAE (11 AWS sites recorded rainfall). Two days later (Fig. 14b), the Arabian heat low is centered at the western edge of the map near 20°N, and the Arabian Gulf circulation is centered over the Strait of Hormuz. This results in onshore flow over the eastern UAE, and consequently, rainfall is prevalent over the eastern UAE.

Figure 15a shows MSLP, 10-m wind vectors, and 2-m specific humidity at 0600 UTC 21 July 2013. With a minimum pressure below 995 hPa, the Arabian heat low is deeper than any cases examined so far. However, only 1.2 mm of rain was recorded at a single site. The Arabian heat low circulation is centered near the southern UAE border, and no separate circulation is present over the Arabian Gulf. Dry air is entrained into the heat low circulation on the western flank, and specific humidity along the western UAE coast is lower than the other cases examined. Figure 15b shows 2-m specific humidity and 10-m wind vectors from WRF simulations at 0900 UTC 21 July 2013. Drier conditions exist offshore, and the moisture field rapidly erodes inland. Figure 15c shows a cross section representing onshore flow at 0900 UTC. Compared to the 30 and 31 August 2011 rain days, the onshore moist flow is drier and shallower than the other days presented here, with a shallower mixed layer and weaker horizontal convective rolls ahead of the SBF. Dry air is being advected over the region and entrained into the PBL, and with warmer air aloft, it takes longer for the mixed layer to grow. These factors result in lower rainfall totals, compared with cases detailed earlier, despite this case having the strongest Arabian heat low circulation.

6. Discussion and conclusions

The climatological and case study analyses presented here show how meteorological features on a larger scale—the southwest Asian monsoon and the AHL—affect the development of deep convection over the

TABLE 1. WRF sounding parameters corresponding to Fig. 12.

Date/time	CAPE (J kg^{-1})	CIN (J kg^{-1})	LFC (m)
0900 UTC 30 Aug 2011	1	38	2865
0900 UTC 31 Aug 2011	2969	<1	2555
1000 UTC 30 Aug 2011	260	<1	3969
1000 UTC 31 Aug 2011	1321	<1	2938

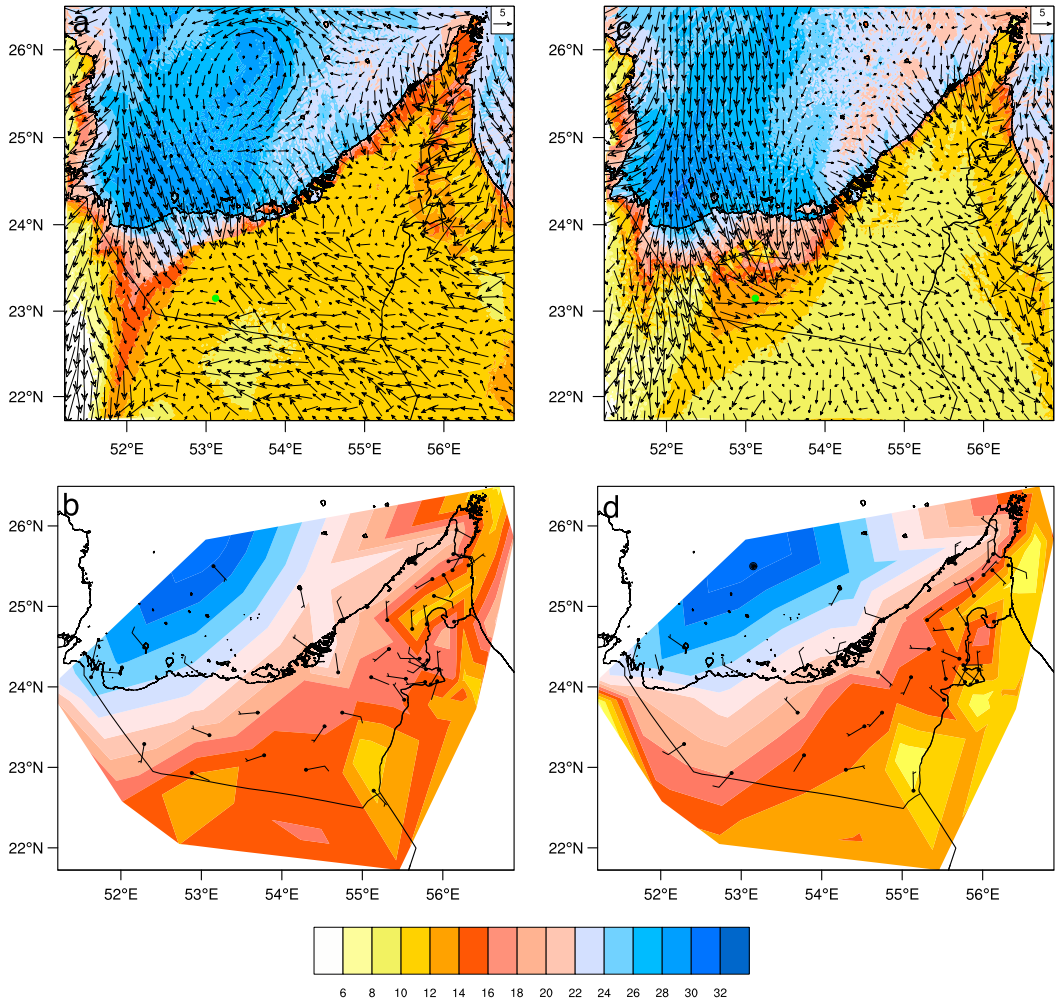

FIG. 13. (a) WRF 2-m specific humidity (color shading; g kg^{-1}) and 10-m wind vectors at 1000 UTC 30 Aug 2011; (b) AWS observations of specific humidity interpolated to a triangular mesh (color shading) and wind vectors at 1000 UTC 30 Aug 2011; (c),(d) As in (a) and (b), respectively, but for 1000 UTC 31 Aug 2011.

UAE. Active phases of the southwest Asian monsoon are associated with increased convection and latent heating over the Arabian Sea. Upper-tropospheric easterlies and large-scale subsidence over the Arabian Peninsula result in an enhanced heat low. Mass convergence into the heat low—primarily from the south—leads to a stronger sea-breeze flow, especially during daytime conditions.

The vorticity analysis for the cases presented here show that the heat low circulation strengthens during the day from convergence and weakens at night due to advection effects and friction, while convergence remains positive. A second cyclonic circulation forms during daytime conditions over the eastern UAE due to the strong convergence of sea-breeze flow from the Arabian Gulf and Gulf of Oman and the primary heat low circulation. During nighttime hours, this circulation propagates westward over the Arabian Gulf. This circulation is important for preconditioning the lower troposphere over portions of the UAE with high specific humidity in two ways. First, the closed cyclonic circulation prevents the inflow of drier continental air over the Arabian Gulf, as evaporative fluxes continue to moisten the boundary layer air. Then, this moist air is advected onshore as part of the cyclonic circulation and later from sea-breeze effects. The early-morning preconditioning of areas $O(100)$ km inland with enhanced moisture, the development of horizontal convective rolls, and the approach of the SBF results in the generation of deep convection.

The potential role of the southwest Asian monsoon in modulating the strength of the AHL has been previously

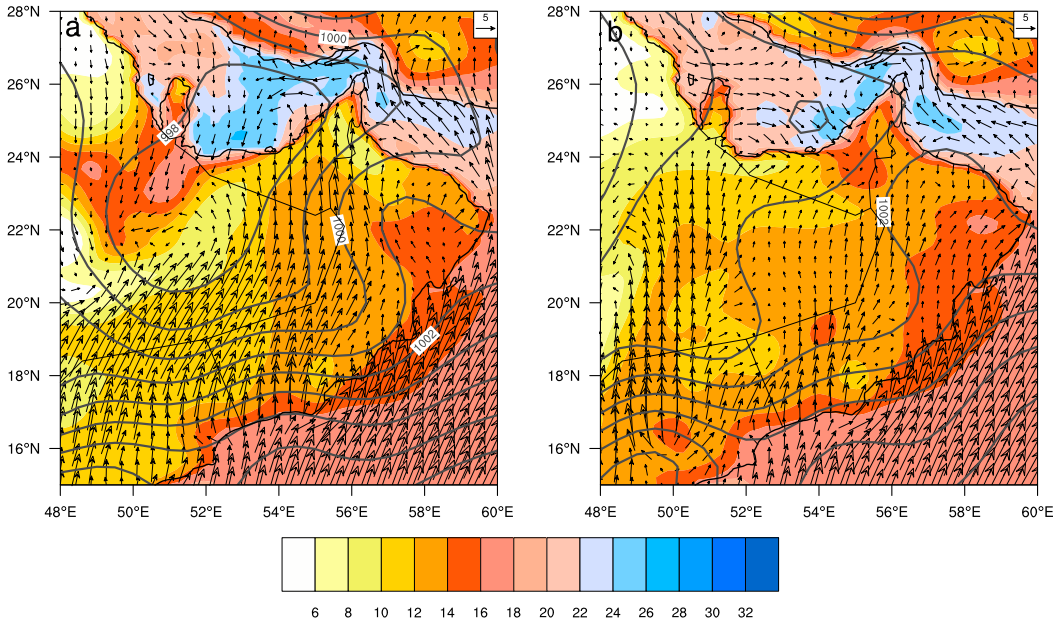

FIG. 14. MSLP (contours; hPa), 2-m specific humidity (color shading; g kg^{-1}), and 10-m wind vectors from CFSR at (a) 0600 UTC 10 Aug and (b) 0600 UTC 12 Aug 2013.

hypothesized (Ramage 1966; Smith 1986a,b), and the results presented here support the hypothesis. A feedback loop can be postulated, based on the aforementioned role of the southwest Asian monsoon on the strength of the AHL and the role of divergent outflow of the AHL near the 850-hPa level toward maintaining monsoon rainfall (e.g., Smith 1986b; Krishnamurti et al. 2013). Further studies using climatological reanalyses and idealized modeling simulations can more clearly demonstrate this connection. The temporal clustering of July–August rainfall days over the western UAE—21 of 40 rain days over the 2003–14 period occur within 2 days of another rain day—suggests the role of active/break periods of the southwest Asian monsoon in modulating the AHL. The high-frequency intraseasonal oscillations (HF-ISO) of monsoon rainfall studied by Karmakar et al. (2017), with periodicities of 10–20 days, may have connections to the rain-day anomalies in Fig. 2. In particular, active rainfall periods over northwestern India and negative geopotential height anomalies in the upper troposphere over Iran that are associated with HF-ISO phases 1, 7, and 8 of Karmakar et al. (2017) are similar to the geopotential height and OLR rain-day anomalies shown in Fig. 2. Of the 12 years included in the present analysis, the 7 years with the most intense HF-ISO indices (Fig. 4a in Karmakar et al. 2017) contain 39 of the 40 rain days.

The AHL is typically characterized by a temporal mean MSLP signature (like that shown in Fig. 2d) and thermodynamic structure that has been well studied. However, as previously mentioned and illustrated here, the heat low is not in quasigeostrophic balance, and both the strength and location of the AHL circulation vary daily. The strength and position of the AHL circulation can influence lower-tropospheric convergence and moisture patterns over much of the Arabian Peninsula, as shown in section 5. Convergence associated with the AHL and sea breeze is primarily responsible for the development of an additional cyclonic circulation over the Arabian Gulf that, to our knowledge, has not been previously discussed. Further studies to characterize the variability of the AHL and the circulation patterns over the Arabian Gulf would benefit understanding of the hydrology of the UAE.

Features associated with deep convection over the UAE were not extensively discussed here, as the proper structure and placement of horizontal convective rolls and the SBF require model simulations with LES PBL formulations and horizontal grid spacing well below 1 km (e.g., Rao et al. 1999; Thurston et al. 2016). However, the simulations of convective initiation associated with the SBF shown here are consistent with the idealized studies of Dailey and Fovell (1999) and Fovell (2005). Convection is initiated above updrafts associated with horizontal convective rolls ahead of the SBF, and the generation of deep convection is dependent upon the ambient conditions ahead of the SBF. The early-morning moisture preconditioning is thus important in the convective initiation ahead of the SBF. Intensification then occurs, associated with obstacle-effect

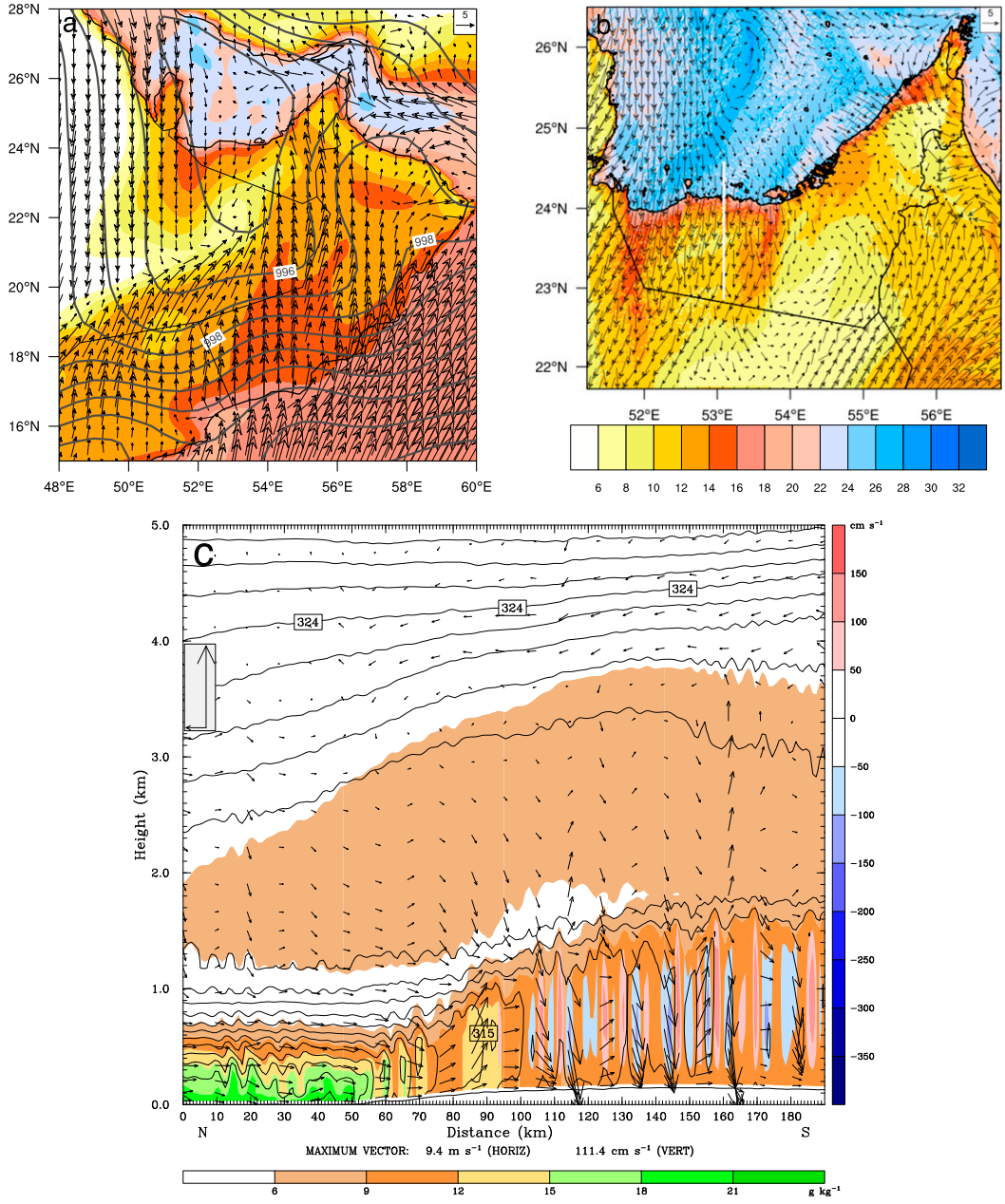

FIG. 15. (a) MSLP (contours; hPa), 2-m specific humidity (color shading; g kg^{-1}), and 10-m wind vectors from CFSR at 0600 UTC 21 Jul 2013; (b) WRF 2-m specific humidity (color shading) and 10-m wind vectors at 0900 UTC 21 Jul 2013; (c) vertical cross-section of potential temperature (contours; K), specific humidity (color shading using scale at bottom of plot; g kg^{-1}), vertical velocity (color shading using scale to right of plot; cm s^{-1}), and circulation vectors (with reference vectors on right edge of plots) corresponding to the white line in (b).

gravity waves and an SBF–horizontal convective roll merger, and deep convection in the simulations presented here occurs behind the SBF. However, additional simulations would be needed to further clarify the meso- and microscale effects related to deep convection over the UAE.

Acknowledgments. Meteorological data and funding for this research were provided by the UAE NCMS, and Penguin on Demand (POD) computing provided preferential cost structures for WRF simulations. The National Center for Atmospheric Research is sponsored by the National Science Foundation. Two anonymous reviewers

provided helpful comments and suggestions toward improving the original manuscript.

REFERENCES

Ackerman, S. A., and S. K. Cox, 1982: The Saudi Arabian heat low: Aerosol distributions and thermodynamic structure. *J. Geophys. Res.*, **87**, 8991–9002, https://doi.org/10.1029/JC087iC11p08991.

Atkins, N. T., R. M. Wakimoto, and T. M. Weckwerth, 1995: Observations of the sea-breeze front during CaPE. Part II: Dual-Doppler and aircraft analysis. *Mon. Wea. Rev.*, **123**, 944–969, https://doi.org/10.1175/1520-0493(1995)123<0944:OOTSBF>2.0.CO;2.

Atkinson, B. W., and J. W. Zhang, 1996: Mesoscale shallow convection in the atmosphere. *Rev. Geophys.*, **34**, 403–431, https://doi.org/10.1029/96RG02623.

Bitan, A., and H. Sa'Aroni, 1992: The horizontal and vertical extension of the Persian Gulf pressure trough. *Int. J. Climatol.*, **12**, 733–747, https://doi.org/10.1002/joc.3370120706.

Blake, D. W., T. N. Krishnamurti, S. V. Low-Nam, and J. S. Fein, 1983: Heat low over the Saudi Arabian desert during May 1979 (summer MONEX). *Mon. Wea. Rev.*, **111**, 1759–1775, https://doi.org/10.1175/1520-0493(1983)111<1759:HLOTSA>2.0.CO;2.

Bollasina, M., and S. Nigam, 2011: The summertime ''heat'' low over Pakistan/northwestern India: Evolution and origin. *Climate Dyn.*, **37**, 957–970, https://doi.org/10.1007/s00382-010-0879-y.

Burton, R. R., A. Gadian, A. M. Blyth, and S. D. Mobbs, 2013: Modelling isolated deep convection: A case study from COPS. *Meteor. Z.*, **22**, 433–443, https://doi.org/10.1127/0941-2948/2013/0408.

Chandran, A., G. Basha, and T. B. M. J. Ouarda, 2016: Influence of climate oscillations on temperature and precipitation over the United Arab Emirates. *Int. J. Climatol.*, **36**, 225–235, https://doi.org/10.1002/joc.4339.

Chen, F., and J. Dudhia, 2001: Coupling an advanced land surface–hydrology model with the Penn State–NCAR MM5 modeling system. Part I: Model implementation and sensitivity. *Mon. Wea. Rev.*, **129**, 569–585, https://doi.org/10.1175/1520-0493(2001)129<0569:CAALSH>2.0.CO;2.

Chen, S. H., and W. Y. Sun, 2001: Application of the multigrid method and a flexible hybrid coordinate in a nonhydrostatic model. *Mon. Wea. Rev.*, **129**, 2660–2676, https://doi.org/10.1175/1520-0493(2001)129<2660:AOTMMA>2.0.CO;2.

Crosman, E. T., and J. D. Horel, 2010: Sea and lake breezes: A review of numerical studies. *Bound.-Layer Meteor.*, **137**, 1–29, https://doi.org/10.1007/s10546-010-9517-9.

Dailey, P. S., and R. G. Fovell, 1999: Numerical simulation of the interaction between the sea-breeze front and horizontal convective rolls. Part I: Offshore ambient flow. *Mon. Wea. Rev.*, **127**, 858–878, https://doi.org/10.1175/1520-0493(1999)127<0858:NSOTIB>2.0.CO;2.

Eager, R. E., S. Raman, A. Wootten, D. L. Westphal, J. S. Reid, and A. Al Mandoos, 2008: A climatological study of the sea and land breezes in the Arabian Gulf region. *J. Geophys. Res.*, **113**, D15106, https://doi.org/10.1029/2007JD009710.

Etling, D., and R. A. Brown, 1993: Roll vortices in the planetary boundary layer: A review. *Bound.-Layer Meteor.*, **65**, 215–248, https://doi.org/10.1007/BF00705527.

FAO, 1997: Irrigation in the Near East region in figures. Water Rep. 9, U.N. Food and Agriculture Organization, 292 pp., http://www.fao.org/docrep/w4356e/.

Fovell, R. G., 2005: Convective initiation ahead of the sea-breeze front. *Mon. Wea. Rev.*, **133**, 264–278, https://doi.org/10.1175/MWR-2852.1.

——, and P. S. Dailey, 2001: Numerical simulation of the interaction between the sea-breeze front and horizontal convective rolls. Part II: Alongshore ambient flow. *Mon. Wea. Rev.*, **129**, 2057–2072, https://doi.org/10.1175/1520-0493(2001)129<2057:NSOTIB>2.0.CO;2.

Gadgil, S., and P. V. Joseph, 2003: On breaks of the Indian monsoon. *J. Earth Syst. Sci.*, **112**, 529–558, https://doi.org/10.1007/BF02709778.

Haynes, P. H., and M. E. McIntyre, 1987: On the evolution of vorticity and potential vorticity in the presence of diabatic heating and frictional or other forces. *J. Atmos. Sci.*, **44**, 828–841, https://doi.org/10.1175/1520-0469(1987)044<0828:OTEOVA>2.0.CO;2.

Holton, J. R., 1992: *An Introduction to Dynamic Meteorology.* Academic Press, 511 pp.

Iacono, M. J., J. S. Delamere, E. J. Mlawer, M. W. Shepard, S. A. Clough, and W. D. Collins, 2008: Radiative forcing by long-lived greenhouse gases: Calculations with the AER radiative transfer models. *J. Geophys. Res.*, **113**, D13103, https://doi.org/10.1029/2008JD009944.

Janjić, Z. I., 1994: The step-mountain Eta Coordinate Model: Further developments of the convection, viscous sublayer, and turbulence closure schemes. *Mon. Wea. Rev.*, **122**, 927–945, https://doi.org/10.1175/1520-0493(1994)122<0927:TSMECM>2.0.CO;2.

Karmakar, N., A. Chakraborty, and R. S. Nanjundiah, 2017: Space–time evolution of the low- and high-frequency intraseasonal modes of the Indian summer monsoon. *Mon. Wea. Rev.*, **145**, 413–435, https://doi.org/10.1175/MWR-D-16-0075.1.

Kilroy, G., R. K. Smith, M. T. Montgomery, B. Lynch, and C. Earl-Spurr, 2016: A case- study of a monsoon low that formed over the sea and intensified over land as seen in ECMWF analyses. *Quart. J. Roy. Meteor. Soc.*, **142**, 2244–2255, https://doi.org/10.1002/qj.2814.

Kleist, D. T., D. F. Parrish, J. C. Derber, R. Treadon, W.-S. Wu, and S. Lord, 2009: Introduction of the GSI into the NCEP Global Data Assimilation System. *Wea. Forecasting*, **24**, 1691–1705, https://doi.org/10.1175/2009WAF2222201.1.

Krishnamurti, T. N., L. Stefanova, and V. Misra, 2013: *Tropical Meteorology.* Springer, 423 pp.

Kumar, K. N., and T. B. M. J. Ouarda, 2014: Precipitation variability over UAE and global SST teleconnections. *J. Geophys. Res. Atmos.*, **119**, 10 313–10 322, https://doi.org/10.1002/2014JD021724.

Lin, Y.-L., R. D. Farley, and H. D. Orville, 1983: Bulk parameterization of the snow field in a cloud model. *J. Climate Appl. Meteor.*, **22**, 1065–1092, https://doi.org/10.1175/1520-0450(1983)022<1065:BPOTSF>2.0.CO;2.

Martin, J. E., 2006: *Mid-latitude Atmospheric Dynamics.* Wiley, 324 pp.

Miller, S. T. K., B. D. Keim, R. W. Talbot, and H. Mao, 2003: Sea breeze: Structure, forecasting, and impacts. *Rev. Geophys.*, **41**, 1011, https://doi.org/10.1029/2003RG000124.

Mohalfi, S., H. S. Bedi, T. N. Krishnamurti, and S. D. Cocke, 1998: Impact of shortwave radiative effects of dust aerosols on the summer season heat low over Saudi Arabia. *Mon. Wea. Rev.*, **126**, 3153–3168, https://doi.org/10.1175/1520-0493(1998)126<3153:IOSREO>2.0.CO;2.

Ouarda, T. B. M. J., C. Charron, K. Niranjan Kumar, P. R. Marpu, H. Ghedira, A. Molini, and I. Khayal, 2014: Evolution of the rainfall regime in the United Arab Emirates. *J. Hydrol.*, **514**, 258–270, https://doi.org/10.1016/j.jhydrol.2014.04.032.

Rácz, Z., and R. K. Smith, 1999: The dynamics of heat lows. *Quart. J. Roy. Meteor. Soc.*, **125**, 225–252, https://doi.org/10.1002/qj.49712555313.

Rajeevan, M., A. Kesarkar, S. B. Thampi, T. N. Rao, B. Radhakrishna, and M. Rajasekhar, 2010: Sensitivity of WRF cloud microphysics to simulations of a severe thunderstorm event over southeast India. *Ann. Geophys.*, **28**, 603–619, https://doi.org/10.5194/angeo-28-603-2010.

Ramage, C. S., 1966: The summer atmospheric circulation over the Arabian Sea. *J. Atmos. Sci.*, **23**, 144–150, https://doi.org/10.1175/1520-0469(1966)023<0144:TSACOT>2.0.CO;2.

Rao, P. A., H. E. Fuelberg, and K. K. Droegemeier, 1999: High-resolution modeling of the Cape Canaveral area land–water circulations and associated features. *Mon. Wea. Rev.*, **127**, 1808–1821, https://doi.org/10.1175/1520-0493(1999)127<1808:HRMOTC>2.0.CO;2.

Raymond, D. J., and C. López-Carrillo, 2011: The vorticity budget of developing Typhoon Nuri (2008). *Atmos. Chem. Phys.*, **11**, 147–163, https://doi.org/10.5194/acp-11-147-2011.

——, S. Gjorgjievska, S. Sessions, and Z. Fuchs, 2014: Tropical cyclogenesis and mid-level vorticity. *Aust. Meteor. Ocean J.*, **64**, 11–25, https://doi.org/10.22499/2.6401.003.

Saha, S., and Coauthors, 2010a: The NCEP Climate Forecast System Reanalysis. *Bull. Amer. Meteor. Soc.*, **91**, 1015–1058, https://doi.org/10.1175/2010BAMS3001.1.

——, and Coauthors, 2010b: NCEP Climate Forecast System Reanalysis (CFSR) 6-hourly products, January 1979 to December 2010. Research Data Archive at the National Center for Atmospheric Research, Computational and Information Systems Laboratory, accessed 21 October 2016, https://doi.org/10.5065/D69K487J.

——, and Coauthors, 2010c: NCEP Climate Forecast System Reanalysis (CFSR) selected hourly time-series products, January 1979 to December 2010. Research Data Archive at the National Center for Atmospheric Research, Computational and Information Systems Laboratory, accessed 21 October 2016, https://doi.org/10.5065/D6513W89.

——, and Coauthors, 2011a: NCEP Climate Forecast System version 2 (CFSv2) 6-hourly products. Research Data Archive at the National Center for Atmospheric Research, Computational and Information Systems Laboratory, accessed 21 October 2016, https://doi.org/10.5065/D61C1TXF.

——, and Coauthors, 2011b: NCEP Climate Forecast System version 2 (CFSv2) selected hourly time-series products. Research Data Archive at the National Center for Atmospheric Research, Computational and Information Systems Laboratory, accessed 21 October 2016, https://doi.org/10.5065/D6N877VB.

——, and Coauthors, 2014: The NCEP Climate Forecast System version 2. *J. Climate*, **27**, 2185–2208, https://doi.org/10.1175/JCLI-D-12-00823.1.

Sherif, M., M. Almulla, A. Shetty, and R. K. Chowdhury, 2014: Analysis of rainfall, PMP and drought in the United Arab Emirates. *Int. J. Climatol.*, **34**, 1318–1328, https://doi.org/10.1002/joc.3768.

Simpson, J. E., 1994: *Sea Breeze and Local Winds*. Cambridge University Press, 234 pp.

Skamarock, W. C., and Coauthors, 2008: A description of the Advanced Research WRF version 3. NCAR Tech. Note NCAR/TN-475+STR, 113 pp., https://doi.org/10.5065/D68S4MVH.

Smith, E. A., 1986a: The structure of the Arabian heat low. Part I: Surface energy budget. *Mon. Wea. Rev.*, **114**, 1067–1083, https://doi.org/10.1175/1520-0493(1986)114<1067:TSOTAH>2.0.CO;2.

——, 1986b: The structure of the Arabian heat low. Part II: Bulk tropospheric heat budget and implications. *Mon. Wea. Rev.*, **114**, 1084–1102, https://doi.org/10.1175/1520-0493(1986)114<1084:TSOTAH>2.0.CO;2.

Smith, R. K., M. T. Montgomery, G. Kilroy, S. Tang, and S. K. Müller, 2015: Tropical low formation during the Australian monsoon: The events of January 2013. *Aust. Meteor. Ocean J.*, **65**, 318–341, https://doi.org/10.22499/2.6503.003.

Spengler, T., and R. K. Smith, 2008: The dynamics of heat lows over flat terrain. *Quart. J. Roy. Meteor. Soc.*, **134**, 2157–2172, https://doi.org/10.1002/qj.342.

Thurston, W., R. J. B. Fawcett, K. J. Tory, and J. D. Kepert, 2016: Simulating boundary- layer rolls with a numerical weather prediction model. *Quart. J. Roy. Meteor. Soc.*, **142**, 211–223, https://doi.org/10.1002/qj.2646.

Tiedtke, M., 1989: A comprehensive mass flux scheme for cumulus parameterization in large-scale models. *Mon. Wea. Rev.*, **117**, 1779–1800, https://doi.org/10.1175/1520-0493(1989)117<1779:ACMFSF>2.0.CO;2.

Tory, K. J., J. D. Kepert, J. A. Sippel, and C. M. Nguyen, 2012: On the use of potential vorticity tendency equations for diagnosing atmospheric dynamics in numerical models. *J. Atmos. Sci.*, **69**, 942–960, https://doi.org/10.1175/JAS-D-10-05005.1.

Wakimoto, R. M., and N. T. Atkins, 1994: Observations of the seabreeze front during CaPE. Part I: Single-Doppler, satellite, and cloud photogrammetry analysis. *Mon. Wea. Rev.*, **122**, 1092–1114, https://doi.org/10.1175/1520-0493(1994)122<1092:OOTSBF>2.0.CO;2.

Warner, T. T., 2004: *Desert Meteorology*. Cambridge University Press, 595 pp.

Weckwerth, T. M., 2000: The effect of small-scale moisture variability on thunderstorm initiation. *Mon. Wea. Rev.*, **128**, 4017–4030, https://doi.org/10.1175/1520-0493(2000)129<4017:TEOSSM>2.0.CO;2.

——, J. W. Wilson, and R. M. Wakimoto, 1996: Thermodynamic variability within the convective boundary layer due to horizontal convective rolls. *Mon. Wea. Rev.*, **124**, 769–784, https://doi.org/10.1175/1520-0493(1996)124<0769:TVWTCB>2.0.CO;2.

——, ——, ——, and N. A. Crook, 1997: Horizontal convective rolls: Determining the environmental conditions supporting their existence and characteristics. *Mon. Wea. Rev.*, **125**, 505–526, https://doi.org/10.1175/1520-0493(1997)125<0505:HCRDTE>2.0.CO;2.

——, T. W. Horst, and J. W. Wilson, 1999: An observational study of the evolution of horizontal convective rolls. *Mon. Wea. Rev.*, **127**, 2160–2179, https://doi.org/10.1175/1520-0493(1999)127<2160:AOSOTE>2.0.CO;2.

Wehbe, Y., D. Ghebreyesus, M. Temimi, A. Milewski, and A. Al Mandous, 2017: Assessment of the consistency among global precipitation products over the United Arab Emirates. *J. Hydrol.: Reg. Stud.*, **12**, 122–135, https://doi.org/10.1016/j.ejrh.2017.05.002.

Young, G. S., D. A. R. Kristovich, M. R. Hjelmfelt, and R. C. Foster, 2002: Rolls, streets, waves, and more: A review of quasi-two-dimensional structures in the atmospheric boundary layer. *Bull. Amer. Meteor. Soc.*, **83**, 997–1002, https://doi.org/10.1175/1520-0477(2002)083<0997:RSWAMA>2.3.CO;2.

Zhang, C., Y. Wang, and K. Hamilton, 2011: Improved representation of boundary layer clouds over the southeast Pacific in ARW-WRF using a modified Tiedtke cumulus parameterization scheme. *Mon. Wea. Rev.*, **139**, 3489–3513, https://doi.org/10.1175/MWR-D-10-05091.1.

Zhu, M., and B. W. Atkinson, 2004: Observed and modelled climatology of the land–sea breeze circulation over the Persian Gulf. *Int. J. Climatol.*, **24**, 883–905, https://doi.org/10.1002/joc.1045.